Vulnerability and high temperatures exacerbate impacts of ongoing drought in Central South America

Paola A. Arias[1] ,Juan Antonio Rivera[2], Anna A. Sörensson [3,4,5], Mariam Zachariah[6], Clair Barnes[6], Sjoukje Philip[7], Sarah Kew[7], Robert Vautard[8], Gerbrand Koren[9], Izidine Pinto[7], Maja Vahlberg[10], Roop Singh[10], Emmanuel Raju[13], Sihan Li[14], Wenchang Yang[15], Gabriel A. Vecchi[15,16], Friederike E.L. Otto[6]

1. Grupo de Ingeniería y Gestión Ambiental (GIGA), Escuela Ambiental, Facultad de Ingeniería, Universidad de Antioquia, Colombia
2. Instituto Argentino de Nivología, Glaciología y Ciencias Ambientales (IANIGLA), CCT CONICET Mendoza, Argentina.
3. Facultad de Ciencias Exactas y Naturales, Universidad de Buenos Aires, Buenos Aires
4. Centro de Investigaciones del Mar y la Atmósfera,CONICET–Universidad de Buenos Aires, Buenos Aires, Argentina
5. CNRS–IRD–CONICET–UBA, Instituto Franco-Argentino para el Estudio del Clima y sus Impactos (IRL 3351 IFAECI), Buenos Aires, Argentina
6. Grantham Institute, Imperial College London, UK
7. Royal Netherlands Meteorological Institute (KNMI), De Bilt, The Netherlands
8. Institut Pierre-Simon Laplace, Paris, France
9. Copernicus Institute of Sustainable Development, Utrecht University, Utrecht, the Netherlands
10. Red Cross Red Crescent Climate Centre, The Hague, the Netherlands
11. Faculty of Geo-Information Science and Earth Observation (ITC), University of Twente, Enschede, the Netherlands
12. Global Disaster Preparedness Center, American Red Cross, Washington DC, USA
13. Department of Public Health, Global Health Section & Copenhagen Centre for Disaster Research
14. Department of Geography, University of Sheffield
15. Department of Geosciences, Princeton University, Princeton, NJ 08544, USA
16. High Meadows Environmental Institute, Princeton University, Princeton, NJ 08544, USA

Main findings

- The ongoing drought has led to severe impacts on agriculture, halving the annual harvests in wheat and soy in Argentina, which in turn is expected to lead to export deficits of 25-50%. The drought impacts hit the population on top of already high inflation and weakening local currency. In Uruguay, more than 75,000 people are suffering from lack of access to potable water; access to water for crops and livestock is also limited.
- Central South America has suffered from drought for the last three years, which saw consecutive La Niña conditions. There is a high correlation between the rainfall deficit in

the study region during the months of October to December and the Niño3.4 index. Thus, the rainfall deficit is in part driven by La Niña.

- In order to identify whether human-induced climate change was also a driver of the rainfall deficit, we analysed rainfall over the most impacted region and in 9 representative stations. For the region as a whole, the event has a return period of 20 years, meaning it has a 5% chance of occurrence in any given year. At individual stations, it is a less common event, with return times up to 50 years.

- In the observations over the whole region we observed a trend of reduced rainfall over the last 40 years, although we cannot be confident that this trend is beyond what is expected from natural variability in the region.

- In order to identify whether the reduced rainfall is a real trend beyond natural variability that can be attributed to climate change, we looked at once in 20-year low rainfall events over the same region in climate models and found that the models show that low rainfall events decrease - ie they become wetter; the opposite of the trend observed in most weather records - although this trend is again not significant and is compatible with natural variability. Thus, we cannot attribute the low rainfall to climate change.

- This does not rule out that climate change affected other aspects of the drought. To investigate whether the high temperatures, which are in part attributable to climate change, led to a deficit in water availability, calculated as potential evapotranspiration subtracted from the rainfall, we repeated the analysis for this indicator.

- The results show that, in climate models, the increase in temperature does partly compensate for the increase in rainfall but only to offset the wettening, and does not lead to a significant climate change signal in effective precipitation..

- However, higher temperatures in the region, which have been attributed to climate change, decreased water availability in the models in late 2022, indicating that climate change probably reduced water availability over this period in the observations too, thus increasing agricultural drought, although the study cannot quantify this effect.

- This means even though the reduced rainfall is within the natural variability, consequences of drought are becoming more severe due to the strong increase in extreme heat.

- The high impact of the drought on agriculture and economic activity speaks to the need to reduce vulnerability to drought in this region. Measures such as improved water efficiency and management, anticipation of drought using seasonal forecasts, and insurance instruments to help farmers weather dry years could improve resilience to these types of events.

1 Introduction

The third La Niña year in a row caused a prolonged period of drought conditions over much of Southeastern South America. Central Argentina recorded in 2022 its driest year since 1960, with Argentina's core crop region experiencing its second driest year after 2008. In particular, drought severity exacerbated during late spring and early summer of 2022/23, causing widespread impacts to the agricultural sector. According to the National Drought Monitoring Board, during September 2022 (MAGYP, 2022a), 53 departments located in the Argentinean Pampas entered under the severe drought category, a situation that put over 12 million cattle and almost 2 million hectares of wheat at risk. The situation worsened during October 2022 (MAGYP, 2022b), with a large portion of central

and northern Argentina being affected by drought conditions, increasing the risk of crop failures to almost 3.5 million hectares and affecting more than 18.5 million cattle. Almost 22 million hectares distributed along five provinces were affected by severe drought conditions during this month (MAGYP, 2022c). November 2022 (MAGYP, 2022d) experienced an increase of 2 million hectares affected by severe drought conditions with respect to the previous month, while December 2022 (MAGYP, 2022e) added 4.5 million hectares more to this category, although crop areas and cattle at risk experienced a reduction. According to the mid-January forecast of crop yields from ProRindes, there is a projected decrease of 25-50% in soy yields over much of Central Argentina. The intensification of the precipitation deficit was also evident over Uruguay during part of spring and summer, with moderate to severe drought conditions between October and December 2022 over much of the country (INUMET, 2022a). The precipitation deficit ranged from -20% in the northwest to -80% in the south during spring (INUMET, 2022b), while December showed an increase in precipitation deficits, with almost all the country experiencing reductions of more than -60% of total precipitation (INUMET, 2022c). Bolivia also experienced severe drought impacts during 2022, with almost 180 municipalities affected by precipitation shortages that threaten food security (Álvarez, 2022). In an effort to minimize the impacts of drought, in November 2022 the bolivian government presented a Plurinational Plan for Immediate Response to Drought, allocating US$ 18 million to secure water provision to the 53 most affected municipalities (MMAYA, 2022). The effect of the prolonged drought on water levels in the major river basins and water management has also impacted other sectors, namely hydropower generation, river-borne food shipments, and freshwater supplies for around 40 million people throughout Argentina, Brazil, and Paraguay (Ionova, 2022). The lower portion of the Paraná River basin experienced a marked decline in water levels since late October (Télam, 2022). Much of the river basins of Uruguay were affected by hydrological drought conditions that generated minimum levels at El Palmar dam (SISSA, 2022). This is particularly relevant given that 30% of the total power generation comes from hydroelectricity. Since 30 January, more than 230 wildfires have burnt over 425.000 hectares across Chile, causing the Chilean government to declare a State of Emergency in the regions of Araucanía, Biobío, and Ñuble (ECHO, 2023; TeleSURtv, 2023). 26 people have died in connection to the fires, making this wildfire season one of the deadliest on record in Chile (NewScientist, 2023).

The recent drought conditions were triggered by several anomalous features of the atmospheric circulation at regional and hemispheric scales. Prevailing convection anomalies were evident along the Western Tropical Pacific Ocean, a region that can trigger wavetrains that favour the establishment of high pressure anomalies over Central South America (Gomes et al., 2021; de Freitas et al., 2023). The anomalous precipitation deficit can also be linked to a reduced moisture transport towards the region, with low specific humidity values and a decrease in the northern flow from the Amazon (Gomes et al., 2021; Marengo et al., 2021). In consequence, several meteorological stations in Central Argentina experienced record low precipitation during the last quarter of 2022 in the context of the last 60 years of records (SMN, 2022a; SMN, 2022b).

The expected far-reaching impact of the drought on crop health and productivity this year is governed by the deficient rainfall in the beginning of the rainy season during October to December, which is the crop growing season in these parts. Therefore for arriving at an event definition, we use the Standardised Precipitation Index for an accumulation period of 3 months (SPI-3). This index is typically used in agricultural drought assessment as it captures the response of rainfall on soil moisture conditions (Mckee et al., 1993). Fig. 1 shows the SPI3-drought classification map based on CPC, CHIRPS and MSWEP datasets for the 2022 OND season, for a large region encompassing the affected regions (5-60°S,30-90°W). The maps are prepared based on US Drought Monitor drought

classifications (D0-abnormally dry, D1-moderate, D2-severe, D3- extreme, and D4-exceptional). See Appendix Table A1 for the classification thresholds and the respective rainfall thresholds for each of the datasets.

We select a spatially and climatologically homogeneous area where the drought was moderate or graver during the three month period from October to November and prone to agricultural loss, as the study region (see blue highlighted area in Fig. 1). The region comprises of southern Brazil (Paraná, Rio Grande do Sul and Santa Catarina provinces), central and northern Argentina (all states to the north of Buenos Aires), Uruguay and the two southernmost provinces of Bolivia (Tarija and Chuquisaca), hereafter referred to as Central South America (CSA). It may be noted that the selected region encompasses the key wheat growing states of Buenos Aires, Córdoba and Santa Fe and the wine-producing regions in northwestern Argentina, both of which industries are threatened by the ongoing drought conditions (Pratt, 2023; Lerner, 2022; Ionova, 2022).

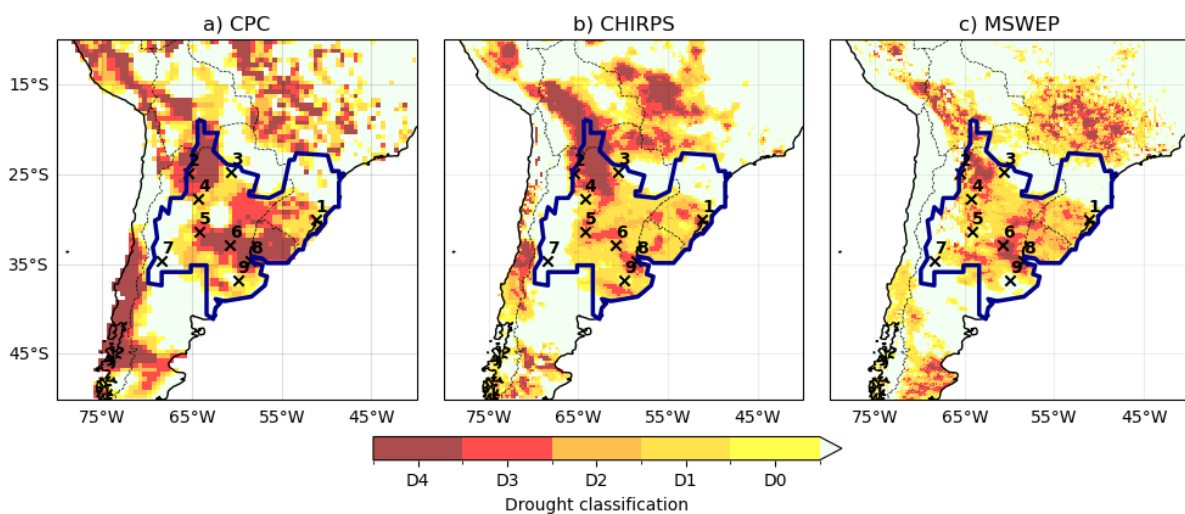*Figure 1: Drought classifications based on 3-month Standardised Precipitation Index (US Drought Monitor, 2023), reflecting the magnitude of the precipitation deficit from Oct-December 2022 relative to the 1980-2010 climatology in three gridded data products. The bold blue outline represents the study region and the crosses mark stations used in the observational analysis: 1. Porto Alegre; 2. Salta; 3. Las Lomitas; 4. Santiago del Estero; 5. Córdoba; 6. Rosario; 7. San Rafael; 8. Buenos Aires; 9. Azul.*

Based on the above observations, for the rest of the study, we define the event by the average precipitation during OND months, and area-averaged over the study region. Given that the season was also anomalously warm and characterised by multiple heatwaves (Rivera et al., 2022), we additionally evaluate the effect of temperature, in particular, whether and to what extent climate change may have influenced the evapotranspiration rates, thereby exacerbating the drought. For this, we consider the effective precipitation during the season, obtained by subtracting the potential evapotranspiration from actual precipitation.

During the last six decades, Southern South America has experienced several prolonged and intense droughts, with widespread impacts on the agricultural and hydrological sectors and, therefore, on the economy and society of the region. The drought events that affected a large portion of the study area were recorded mainly during the decade of 1960 and the first half of the 1970s, but also during the years 1988-89; 1995-96; 2006; 2008-09; 2011; 2017-18 and 2019-22 (Rivera and Penalba, 2014; Naumann et al., 2019). The 1988-89 drought had significant impacts in the economic sector of

Argentina and Uruguay, with severe agricultural production losses, high mortality of animals and minimum levels of hydroelectric power generation (Rivera and Penalba, 2014, Cruz et al., 2018). During the 2008-09 event, more than half of the total population of Argentina and almost 30% of the agricultural land was affected (Naumann et al., 2019). The severity of the 2008-09 drought was the highest recorded since 1935, when the "Pampas Dust Bowl" took place (Tripaldi et al., 2013). The direct agricultural losses reached about 3% of the GDP of Uruguay, although the estimated total losses (direct and indirect) for the Uruguayan economy tripled that value (Cruz et al., 2018). Direct production losses for maize and soybean in Argentina during the 2017-18 flash drought episode were estimated at US$ 1550 million, with an overall impact of about US$ 4600 million to the Argentine economy (Bert et al., 2021). In Uruguay, the estimated national loss due to lower soybean yields was slightly more than US$ 445 million (Hernández et al., 2018).

Most of the historical drought events over the region, including the 2022 event are linked to the El Niño-Southern Oscillation (ENSO) phenomenon, in particular to the La Niña phase characterised by low values of the relative NINO3.4 index (van Oldenborgh et al, 2021): the high positive correlations between precipitation over the study area and this index are shown in Figure 2. The precipitation deficit in response to La Niña events and its impacts on agriculture in the study area have been extensively analysed (Barrucand et al., 2007; Minetti et al., 2007; Penalba and Rivera, 2016; Anderson et al., 2017). However, the ENSO cold phase does not always lead to intense droughts over the region (Sgroi et al., 2021). Other factors, such as the development of blocking conditions over the Southern Pacific Ocean (Alessandro, 2008), warm SST anomalies over tropical North Atlantic (Mo and Berbery, 2011), and other regional and local factors can contribute to the onset and intensification of drought events over the study area. For example, there is a higher sensitivity of the evapotranspiration to changes in soil moisture content when the soil is dry (Ruscica et al., 2014).
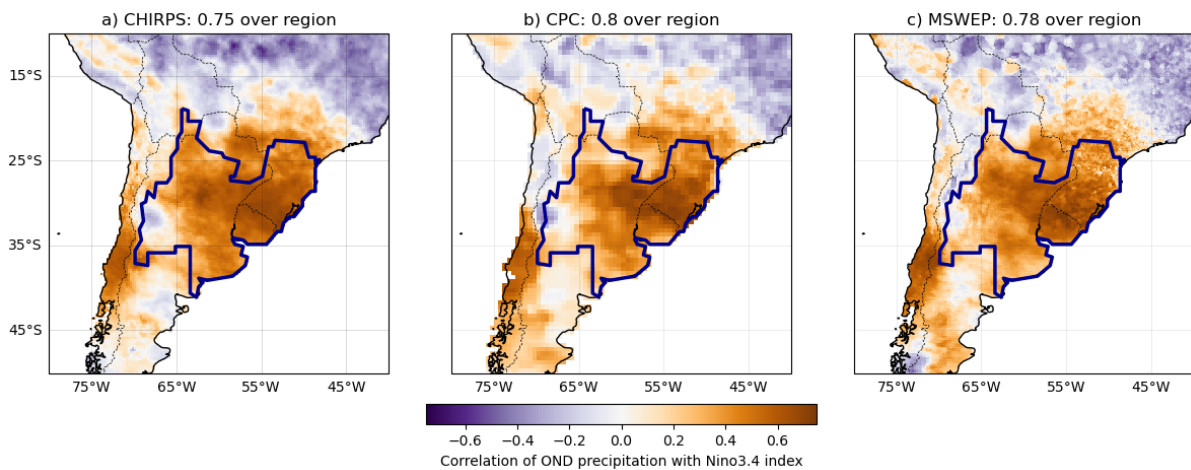

Figure 2: Correlation between October-December precipitation in gridded data products and relative Nino3.4 index, with the study region marked by the bold blue outline. Positive correlations indicate lower precipitation during the La Niña phase of the oscillation.

Different studies have shown that droughts can be triggered or exacerbated by changes in atmospheric moisture transport (Feng et al., 2011; Drumond et al., 2016, 2017, 2019, 2021; Sori et al., 2017; Salah et al., 2018; Stojanovic et al., 2018a, 2018b; Miralles et al., 2019). The main moisture sources for Southern South America, especially the La Plata Basin (LPB), are the terrestrial sources, including local recycling (with a contribution of about 23% of the mean annual precipitation in the region) and the southern Amazon (contributing about 20%) (Martinez and Dominguez, 2014; Zemp et al., 2014).

In particular, the moisture transported from the southern Amazon during the dry season is more efficiently converted to precipitation over LPB than that originated in LPB itself (i.e recycling) (Martinez and Dominguez, 2014). Drumond et al. (2019) analysed the links between anomalous moisture transport and droughts in Southern South America, finding that for instance, the 2008-09 drought was associated with reductions of moisture contributions from terrestrial sources, including the southern Amazon. This suggests that the reduction of atmospheric moisture transported from the southern Amazon could be an important contributor to the precipitation deficits during drought events in LPB.

Deforestation of the Amazon forests, particularly in the southern Amazon, is a driver of reductions of not only local atmospheric moisture recycling but also atmospheric moisture transport toward other regions (e.g. Zemp et al., 2014; Molina et al., 2019; Ruiz-Vasquez et al., 2020). For instance, Ruiz-Vasquez et al. (2020) show that scenarios with deforested areas about 28%-38% in the Amazon exhibit reduced contributions of water vapour toward northern South America of about 40%-43%. Based on the analysis of climatological cascading moisture recycling, Zemp et al. (2014) discuss that the land use change in the Amazon might have a stronger impact on LPB rainfall than previously considered. This suggests that Amazon deforestation could play a role in precipitation deficits over LPB due to reductions of the atmospheric moisture that originates in the Amazon and is transported by the winds toward LPB. This is particularly important in the case of the 2022-23 drought in Southeastern South America, given the fact that the Brazilian Amazon deforestation rate in 2020 was the greatest of the last decade (Silva Junior et al., 2021).

2 Data and methods

The available station data begin in around 1960, with gridded datasets available from around 1980 onwards. Therefore, we use observed records of precipitation and temperature from more than one dataset in this study, for finding the best-fit distribution and estimating return periods, as accurately as possible. As discussed earlier, in addition to precipitation, we consider the effective precipitation (obtained after subtracting the potential evapotranspiration), for evaluating the effect of climate change on the amount of water actually reaching the soil. However, due to challenges associated with observed data products for PET due to (i) unavailability of real-time observed data- e,g., satellite-based GLEAM data product is available only until 2021 December, and (ii) large uncertainties in the monthly anomalies from different observed data products over South America (see Fig. 8 in Sörensson and Ruscica (2018)), we limit this analysis to climate models only.

2.1 Observational data

2.1.1. Station Data

The station data over the study region was provided by the Regional Climate Center Network for Southern South America (CRC-SAS). The CRC-SAS offers climate services in support of the National Meteorological and Hydrometeorological Services and other users from Argentina, Bolivia, Brazil, Chile, Paraguay and Uruguay. From the original dataset, consisting of 454 meteorological stations with precipitation and temperature records spanning the period 1961-2022, we selected 9 representative stations (Azul, Buenos Aires, Córdoba, Las Lomitas, Porto Alegre, Rosario, Salta, San Rafael and Santiago del Estero) located over the region with higher drought severity.

1. ERA5: The European Centre for Medium-Range Weather Forecasts, or the ERA5 reanalysis product begins in the year 1950 (Hersbach et al., 2020). We use precipitation and temperature data from this product. It should be noted that the variables from ERA5 are not directly assimilated, but these are generated by atmospheric components of the Integrated Forecast System (IFS) modelling system.

2. CPC: The CPC Global Unified Gauge-Based Analysis product that is provided by the NOAA PSL, Boulder, Colorado, USA has daily gridded observations for precipitation, maximum and minimum temperature, available at 0.5° x 0.5° resolution, for the period 1979-present.

3. MSWEP: The Multi-Source Weighted-Ensemble Precipitation (MSWEP) v2.8 dataset (updated from Beck et al., 2019) is fully global, available at 3-hourly intervals, and at 0.1° spatial resolution, available from 1979 to ~3 hours from real-time. This product combines gauge-, satellite-, and reanalysis-based data for reliable precipitation estimates, globally.

2.1.2. Observed global mean surface temperature

As a measure of anthropogenic climate change we use the (low-pass filtered) global mean surface temperature (GMST), where GMST is taken from the National Aeronautics and Space Administration (NASA) Goddard Institute for Space Science (GISS) surface temperature analysis (GISTEMP, Hansen et al., 2010 and Lenssen et al. 2019).

2.2 Model and experiment descriptions

We use multiple climate model ensembles from climate modelling experiments that use very different framings (Philip et al., 2020): Sea Surface temperature (SST) driven global circulation high resolution models, coupled global circulation models and regional climate models, as described below.

1. Coordinated Regional Climate Downscaling Experiment CORDEX-CORE multi-model ensemble (Gutowski et al., 2016; Giorgi et al., 2021), comprising simulations resulting from pairings of Global Climate Models (GCMs) and Regional Climate Models (RCMs). These simulations are composed of historical simulations up to 2005, and extended to the year 2100 using the RCP8.5 scenario. For the region considered in this study, twelve model runs are available at 0.44° resolution (SAM-44 domain); and six model runs at 0.22° resolution (SAM-22 domain).

2. The FLOR (Vecchi et al. 2014) and AM2.5C360 (Yang et al. 2021, Chan et al. 2021) climate models are developed at Geophysical Fluid Dynamics Laboratory (GFDL). The FLOR model is an atmosphere-ocean coupled GCM with a resolution of 50 km for land and atmosphere and 1 degree for ocean and ice. Ten ensemble simulations from FLOR are analysed, which cover the period from 1860 to 2100 and include both the historical and RCP4.5 experiments driven by transient radiative forcings from CMIP5 (Taylor et al. 2012). The AM2.5C360 is an atmospheric GCM based on that in the FLOR model (Delworth et al. 2012, Vecchi et al. 2014) with a horizontal resolution of 25 km. Three ensemble simulations of the Atmospheric Model Intercomparison Project (AMIP) experiment (1871-2050) are analysed. These simulations are initialised from three different pre-industrial

conditions but forced by the same SSTs from HadISST1 ([Rayner et al. 2003](#)) after groupwise adjustments ([Chan et al. 2021](#)) over 1871-2020. SSTs between 2021 and 2050 are using the FLOR RCP4.5 experiment 10-ensemble mean values after bias correction. Radiative forcings are using historical values over 1871-2014 and RCP4.5 values after that.

3. CMIP6. This consists of simulations from 27 participating models with varying resolutions. For more details on CMIP6, please see [Eyring et al., (2016)](#). For all simulations, the period 1850 to 2015 is based on historical simulations, while the SSP5-8.5 scenario is used for the remainder of the 21st century.

4. HighResMIP SST-forced model ensemble ([Haarsma et al. 2016](#)), the simulations for which span from 1950 to 2050. The SST and sea ice forcings for the period 1950-2014 are obtained from the 0.25° x 0.25° Hadley Centre Global Sea Ice and Sea Surface Temperature dataset that have undergone area-weighted regridding to match the climate model resolution (see Table B). For the 'future' time period (2015-2050), SST/sea-ice data are derived from RCP8.5 (CMIP5) data, and combined with greenhouse gas forcings from SSP5-8.5 (CMIP6) simulations (see Section 3.3 of Haarsma et al. 2016 for further details).

5. UKCP18 land-GCM: This is a fifteen-member perturbed physics ensemble developed by the UK Met Office ([Murphy et al., 2018](#)). The ensemble members are derived from HadGEM3-GC3.05, a high-resolution coupled ocean-atmosphere model with horizontal grid spacing of approximately 60km at mid-latitudes, which includes an explicit representation of atmospheric aerosols.

2.3 Statistical methods

In this analysis we analyse time series from the CSA region, of precipitation, temperature and effective precipitation for the OND season, where long records of observed data are available. Methods for observational and model analysis and for model evaluation and synthesis are used according to the World Weather Attribution Protocol, described in [Philip et al. (2020)](#), with supporting details found in van [Oldenborgh et al. (2021)](#), [Ciavarella et al. (2021)](#) and [here](#).

The analysis steps include: (i) trend calculation from observations; (ii) model validation; (iii) multi-method multi-model attribution and (iv) synthesis of the attribution statement.
We calculate the return periods, Probability Ratio (PR; the factor-change in the event's probability) and change in intensity of the event under study in order to compare the climate of now and the climate of the past, defined respectively by the GMST values of now and of the preindustrial past (1850-1900, based on the [Global Warming Index](#) (GWI)). The difference in GMST level between the current climate and the climate of the past based on this GWI is 1.2 ℃.

To statistically model the precipitation associated with the event under study, we use a Gaussian distribution that scales with GMST for log transformed precipitation. For modelling the temperature and effective precipitation, we use a Gaussian distribution that shifts with GMST. Next, results from observations and models that pass the validation tests are synthesized into a single attribution statement.

3 Observational analysis: return period and trend

3.1 Analysis of point station data

Fig. 3 shows the trend fitting methods described in [Philip et al. (2020)](#) applied to average OND season log-transformed rainfall for the nine selected stations situated across the CSA domain (Section 2.1.1; Fig. 1). The behaviour of the location parameter with respect to the GMST shows mixed trends at the different stations (Fig. 3). Rainfall at (1) Porto Alegre, and (3) Las Lomitas is found to increase with GMST, whereas at (2) Salta, (5) Córdoba and (9) Azul, it is found to decrease. No trend is discernible at the remaining stations examined. Figure 4 shows the return period plots for log-transformed precipitation at each of these stations the current climate The return period of the 2022 rainfall event in the current climate ranges from 1 to 51 years at these stations (Fig. 4).
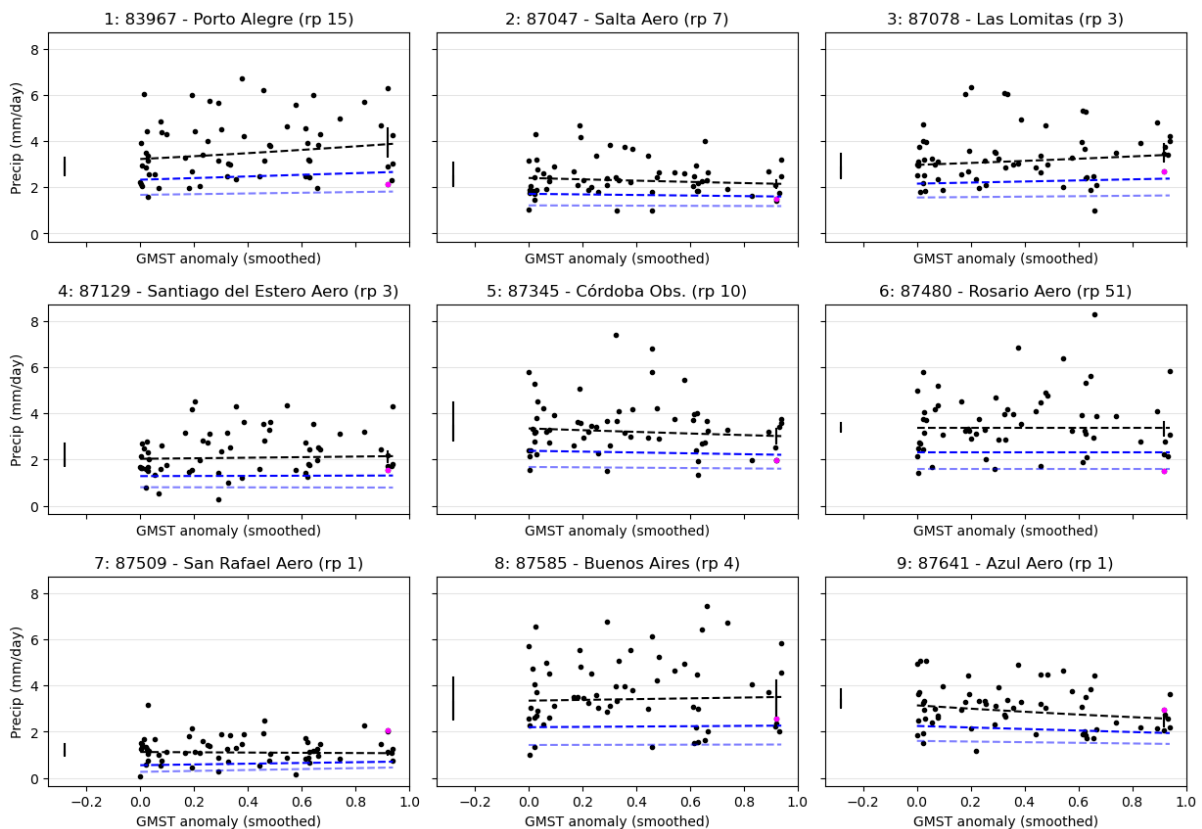
Figure 3: Fitted trends in log-transformed OND precipitation at the nine selected stations with respect to smoothed GMST. Results are transformed back to native rainfall units of mm/day. The dots represent observed OND values, with the 2022 event highlighted in magenta. The dotted black line shows the centre of the distribution, and the blue lines represent the estimated 6-year and 40-year return levels over time. The vertical lines indicate the uncertainty about the location of the centre of the distribution in the current climate and in a 1.2°C cooler climate. Return periods of the 2022 event are given in brackets.

Figure 4: Gaussian-based return periods of log-transformed rainfall for the 2022 climate (red lines) and the 1.2°C cooler climate (blue lines with 95% CI), at the 9 selected stations. The observed event value is shown by the horizontal magenta line.

3.2 Analysis of gridded data

Fig. 5 shows the trend-fitting results for the OND precipitation, area-averaged over CSA, based on three gridded datasets- CHIRPS (Fig. 5(a)), CPC (Fig. 5(b)) and MSWEP (Fig. 5(c)). The left panels show the log-transformed variable as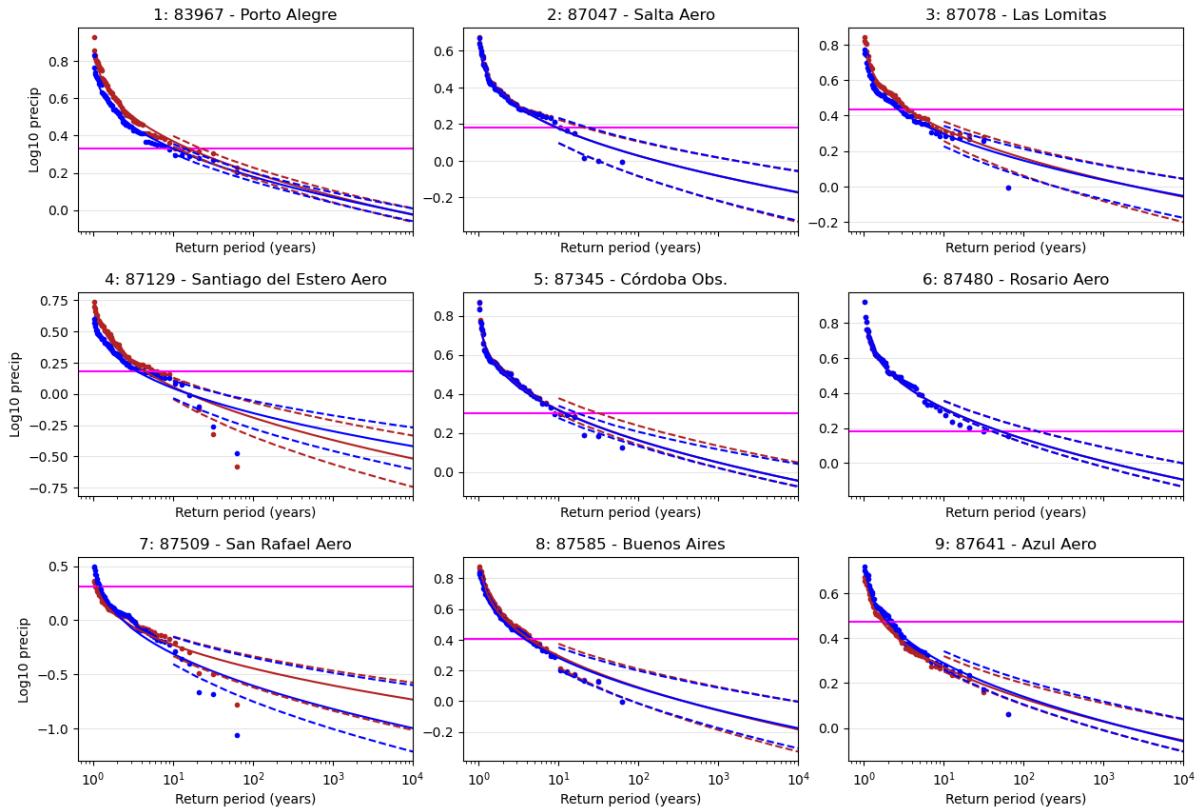 a function of the GMST anomaly, while the right panels show the Gaussian distribution-based return period curves for the log-transformed variable in the present 2022 climate (red lines) and the past climate when the global mean temperature was 1.2°C cooler (blue lines) for the respective datasets. Due to the short data length (42-44 years) and the variability in the rainfall, two of the datasets (CPC and MSWEP) show a decreasing trend in rainfall whereas it is not discernible for CHIRPS. The best-estimated return period of the 2022 event is 20, 30 and 14 years, for the respective datasets, as shown in the right panels of Fig. 5.Since none of the datasets are long enough to estimate the return period with enough confidence, we round these to an average 1-in-20 years for the attribution analysis. The drought is 5 times and 3 times more likely in the 2022 climate, from the CPC and MSWEP datasets, respectively. However, these are not statistically significant, with uncertainty bands of [0.4,135] and [0.3 and 52], respectively. The respective intensity changes of -15% and -13% imply that the 2022 drought is made drier by these amounts due to climate change.

(a) From CHIRPS

(b) From CPC

(c) From MSWEP

Figure 5: (a left) Response of OND rainfall (log-transformed), averaged over the CSA region to change in global mean temperature, based on CHIRPS dataset (left). The thick red line denotes the time-varying mean, and the thin red lines show 1 standard deviation (s.d) and 2 s.d above. The vertical red lines show the 95% confidence interval for the location parameter, for the current, 2022 climate and the hypothetical, 1.2℃ cooler climate. The 2022 observation is highlighted with the magenta box. (a right)Gaussian-based return periods of log-transformed rainfall for the 2022 climate (red lines) and the 1.2℃ cooler climate (blue lines with 95% CI), based on CHIRPS dataset. (b left & right) same as (a), based on CPC dataset. (c left & right) same as (a), based on MSWEP dataset.

Figure 6 shows similar plots for the OND average temperature, area-averaged over the study region, based on two gridded data products- CPC and ERA5. From both datasets, the 2022 temperature is approximately a 1-in-2 year event in the current climate (right panels in Fig. 6).

(a) From CPC

(b) From ERA5

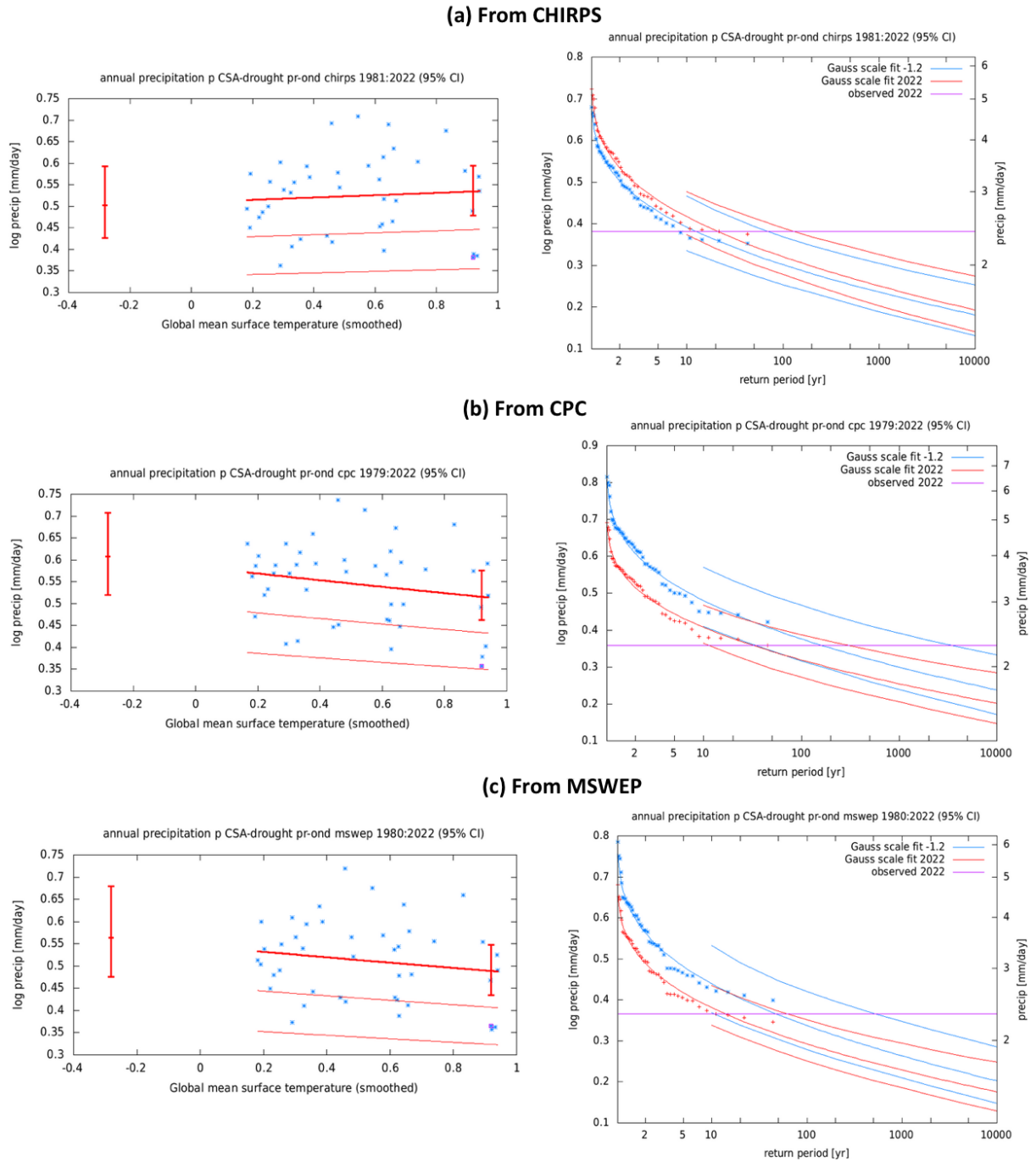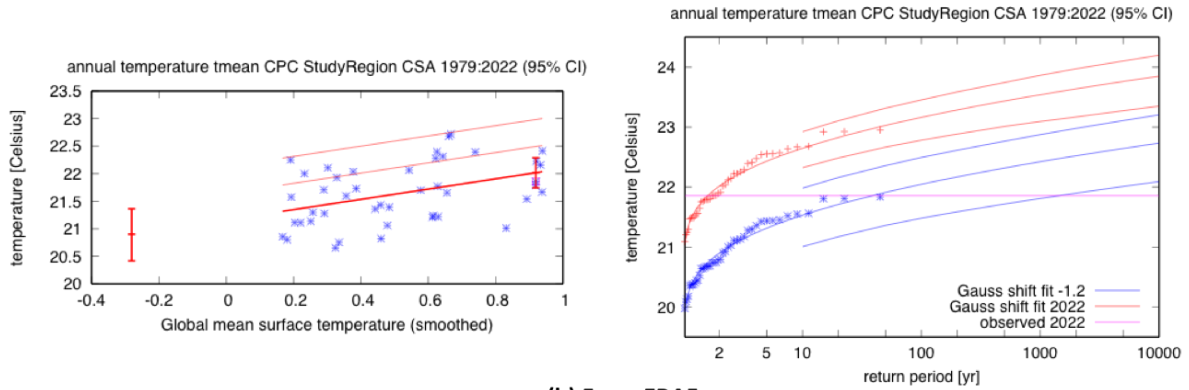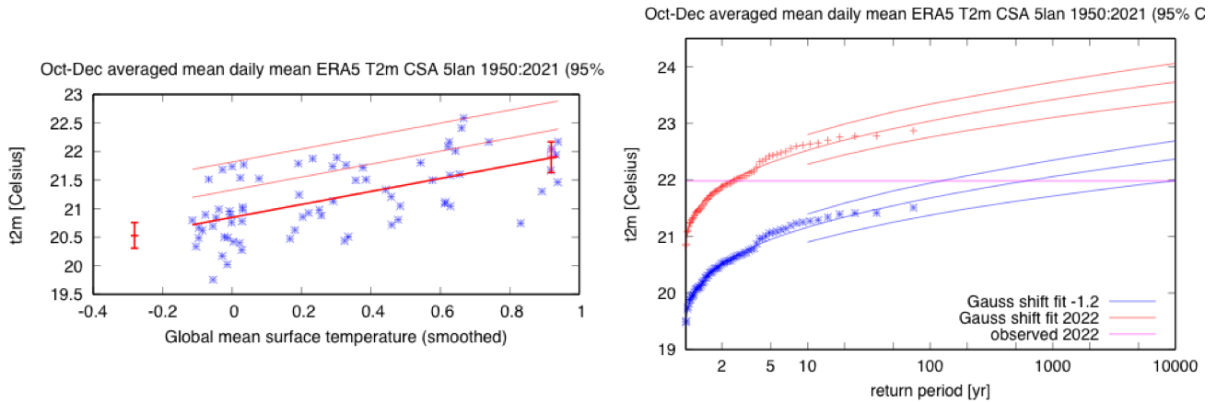*Figure 6: (a left) Response of OND average temperature, averaged over the CSA region to change in global mean temperature, based on CPC dataset (left). The thick red line denotes the time-varying mean, and the thin red lines show 1 standard deviation (s.d) and 2 s.d above. The vertical red lines show the 95% confidence interval for the location parameter, for the current, 2022 climate and the hypothetical, 1.2°C cooler climate. The 2022 observation is highlighted with the magenta box. (a right) Gaussian-based return periods of OND average temperature for the 2022 climate (red lines) and the 1.2°C cooler climate (blue lines with 95% CI), based on CPC dataset. (b left & right) same as (a), based on ERA5 dataset.*

4 Model evaluation

In the subsections below we show the results of the model validation for the CSA region, for precipitation (Table 1) and temperature (Table 2). Due to limitations in observed evapotranspiration products (discussed in Section 2), we do not validate the models for the effective precipitation. Instead, we choose those models that pass the validation for both precipitation and temperature for attribution analysis of this variable. Per framing or model setup we also use models that only just pass the validation tests if we only have five models or less for that framing that perform well. The tables show the model validation results. The climate models are evaluated against the observations in their ability to capture:

1. Seasonal cycles: For this, we qualitatively compare the model outputs against observations-based plots. We discard the models that exhibit multi-modality and/or ill-defined peaks in their seasonal cycles. We also discard the model if the rainy season onset/termination varies significantly from the observations.

2. Spatial patterns: Models that do not match the observations in terms of the large-scale precipitation patterns are excluded.

3. Parameters of the fitted Gaussian/GEV models. We discard the model if the model and observation parameters ranges do not overlap.

The models are labelled as 'good','reasonable', or 'bad' based on their performances in terms of the three criteria discussed above.

*Table 1: Evaluation results for the climate models considered for the attribution analysis of **OND precipitation for CSA region**. The table contains qualitative assessments of seasonal cycle and spatial pattern of precipitation from the models (good, reasonable, bad) along with estimates for dispersion parameter and event magnitude. The corresponding estimates for observations are shown in blue. Based on overall suitability, the models are classified as good, reasonable and bad, shown by green, yellow and red highlights, respectively.*

		Precipitation		
Observations			**Sigma**	**Event magnitude**
CHIRPS			-0.172 (-0.197 ... -0.136)	
MSWEP			-0.172 (-0.195 ... -0.140)	
CPC			-0.164 (-0.191 ... -0.128)	
Models	**Seasonal cycle**	**Spatial pattern**	**Sigma**	**Threshold for 20 year return period (mm/day)**
FLOR historical-rcp4.5 (10)	good	good	-0.167 (-0.181 ... -0.158)	2.258
AM2.5C360 amipHistorical+rcp4.5SST (3)	good	good	-0.170 (-0.193 ... -0.141)	2.239
SAM-22_MOHC-HadGEM2-ES_rcp85_r1i1p1_GERICS-REMO2015 ()	good	good	0.0763 (0.0606 ... 0.0867)	4.135
SAM-22_MOHC-HadGEM2-ES_rcp85_r1i1p1_ICTP-RegCM4-7 ()	good	good	0.112 (0.0881 ... 0.131)	3.466
SAM-22_MPI-M-MPI-ESM-LR_rcp85_r1i1p1_GERICS-REMO2015 ()	reasonable	good	0.142 (0.113 ... 0.163)	2.912
SAM-22_MPI-M-MPI-ESM-MR_rcp85_r1i1p1_ICTP-RegCM4-7 ()	reasonable	good	0.189 (0.148 ... 0.217)	2.102
SAM-22_NCC-NorESM1-M_rcp85_r1i1p1_GERICS-REMO2015 ()	good	good	0.0762 (0.0599 ... 0.0885)	4.446
SAM-22_NCC-NorESM1-M_rcp85_r1i1p1_ICTP-RegCM4-7 ()	good	good	0.108 (0.0822 ... 0.129)	3.778

SAM-44_CCCma-CanESM2_rcp85_r1i1p1_SMHI-RCA4 ()	good	reasonable	0.102 (0.0810 ... 0.117)	2.924
SAM-44_CCCma-CanESM2_rcp85_r1i1p1_UCAN-WRF341I ()	good	good	0.0847 (0.0659 ... 0.102)	3.522
SAM-44_CNRM-CERFACS-CNRM-CM5_rcp85_r1i1p1_SMHI-RCA4 ()	good	reasonable	0.268 (0.215 ... 0.307)	1.493
SAM-44_CSIRO-QCCCE-CSIRO-Mk3-6-0_rcp85_r1i1p1_SMHI-RCA4 ()	reasonable	reasonable	0.109 (0.0761 ... 0.133)	2.647
SAM-44_ICHEC-EC-EARTH_rcp85_r12i1p1_SMHI-RCA4 ()	good	reasonable	0.185 (0.139 ... 0.222)	1.587
SAM-44_IPSL-IPSL-CM5A-MR_rcp85_r1i1p1_SMHI-RCA4 ()	reasonable	reasonable	0.119 (0.0867 ... 0.140)	2.216
SAM-44_MIROC-MIROC5_rcp85_r1i1p1_SMHI-RCA4 ()	good	reasonable	0.195 (0.150 ... 0.230)	2.120
SAM-44_MOHC-HadGEM2-ES_rcp85_r1i1p1_SMHI-RCA4 ()	good	reasonable	0.150 (0.119 ... 0.178)	2.412
SAM-44_MPI-M-MPI-ESM-LR_rcp85_r1i1p1_MPI-CSC-REMO2009 ()	reasonable	good	0.129 (0.0982 ... 0.150)	2.945
SAM-44_MPI-M-MPI-ESM-LR_rcp85_r1i1p1_SMHI-RCA4 ()	good	reasonable	0.316 (0.221 ... 0.408)	1.517
SAM-44_NCC-NorESM1-M_rcp85_r1i1p1_SMHI-RCA4 ()	good	reasonable	0.116 (0.0859 ... 0.141)	2.948
SAM-44_NOAA-GFDL-GFDL-ESM2M_rcp85_r1i1p1_SMHI-RCA4 ()	good	good	0.186 (0.140 ... 0.219)	2.018
ACCESS-CM2_r1i1p1f1 ()	<not computed>	<not computed>	0.0840 (0.0640 ... 0.0990)	2.51
ACCESS-ESM1-5_r1i1p1f1 ()	<not computed>	<not computed>	0.0810 (0.0630 ... 0.0930)	4.37
CanESM5_r1i1p1f1 ()	<not computed>	<not computed>	0.0870 (0.0600 ... 0.108)	3.47
CMCC-ESM2_r1i1p1f1 ()	<not computed>	<not computed>	0.0800 (0.0590 ... 0.0970)	3.89
CNRM-CM6-1-HR_r1i1p1f2 ()	good	reasonable	0.158 (0.123 ... 0.186)	2.14
CNRM-CM6-1_r1i1p1f2 ()	reasonable	good	0.165 (0.125 ... 0.197)	2.57
CNRM-ESM2-1_r1i1p1f2 ()	reasonable	reasonable	0.175 (0.100 ... 0.242)	2.40
EC-Earth3_r1i1p1f1 ()	<not computed>	<not computed>	0.0710 (0.0550 ... 0.0830)	4.17
EC-Earth3-CC_r1i1p1f1 ()	<not computed>	<not computed>	0.0720 (0.0560 ... 0.0840)	4.27
EC-Earth3-Veg_r1i1p1f1 ()	<not computed>	<not computed>	0.0760 (0.0560 ... 0.0950)	3.80

EC-Earth3-Veg-LR_r1i1p1f1 ()	<not computed>	<not computed>	0.0660 (0.0500 ... 0.0760)	3.98
FGOALS-g3_r1i1p1f1 ()	<not computed>	<not computed>	0.0780 (0.0620 ... 0.0900)	2.75
HadGEM3-GC31-LL_r1i1p1f3 ()	<not computed>	<not computed>	0.0580 (0.0450 ... 0.0690)	2.57
HadGEM3-GC31-MM_r1i1p1f3 ()	<not computed>	<not computed>	0.0840 (0.0600 ... 0.106)	4.27
INM-CM4-8_r1i1p1f1 ()	good	good	0.119 (0.0820 ... 0.148)	2.57
INM-CM5-0_r1i1p1f1 ()	<not computed>	<not computed>	0.0790 (0.0640 ... 0.0900)	3.09
IPSL-CM6A-LR_r1i1p1f1 ()	good	reasonable	0.110 (0.0830 ... 0.133)	2.69
KACE-1-0-G_r1i1p1f1 ()	<not computed>	<not computed>	0.0810 (0.0620 ... 0.0940)	2.29
MIROC6_r1i1p1f1 ()	good	good	0.133 (0.0960 ... 0.163)	2.63
MPI-ESM1-2-HR_r1i1p1f1 ()	<not computed>	<not computed>	0.102 (0.0780 ... 0.119)	3.24
MPI-ESM1-2-LR_r1i1p1f1 ()	reasonable	reasonable	0.115 (0.0900 ... 0.135)	3.02
MRI-ESM2-0_r1i1p1f1 ()	good	good	0.171 (0.124 ... 0.208)	2.34
NESM3_r1i1p1f1 ()	<not computed>	<not computed>	0.112 (0.0870 ... 0.129)	2.57
NorESM2-LM_r1i1p1f1 ()	reasonable	good	0.178 (0.135 ... 0.213)	2.29
NorESM2-MM_r1i1p1f1 ()	good	good	0.188 (0.147 ... 0.218)	2.34
TaiESM1_r1i1p1f1 ()	<not computed>	<not computed>	0.0640 (0.0490 ... 0.0750)	3.98
UKESM1-0-LL_r1i1p1f2 ()	<not computed>	<not computed>	0.0710 (0.0530 ... 0.0840)	2.57
ukcp-land-gcm_01 ()	good	good	0.104 (0.0808 ... 0.121)	4.146
ukcp-land-gcm_02 ()	good	good	0.106 (0.0805 ... 0.129)	3.918
ukcp-land-gcm_03 ()	good	good	0.0878 (0.0683 ... 0.101)	3.773
ukcp-land-gcm_04 ()	good	good	0.0738 (0.0551 ... 0.0861)	4.264
ukcp-land-gcm_05 ()	good	good	0.0933 (0.0702 ... 0.112)	3.944

ukcp-land-gcm_06 ()	good	good	0.0839 (0.0630 ... 0.101)	3.987
ukcp-land-gcm_07 ()	good	good	0.111 (0.0829 ... 0.133)	3.711
ukcp-land-gcm_08 ()	good	good	0.116 (0.0843 ... 0.140)	3.268
ukcp-land-gcm_09 ()	good	good	0.0849 (0.0654 ... 0.0989)	3.882
ukcp-land-gcm_10 ()	good	good	0.0859 (0.0593 ... 0.112)	3.986
ukcp-land-gcm_11 ()	good	good	0.0778 (0.0559 ... 0.0991)	3.743
ukcp-land-gcm_12 ()	good	good	0.112 (0.0906 ... 0.126)	3.133
ukcp-land-gcm_13 ()	good	good	0.0750 (0.0587 ... 0.0875)	3.914
ukcp-land-gcm_14 ()	good	good	0.101 (0.0690 ... 0.127)	3.874
ukcp-land-gcm_15 ()	good	good	0.0561 (0.0415 ... 0.0664)	3.800
highresSST_CMCC-CM2-HR4 ()			0.0664 (0.0514 ... 0.0762)	3.683
highresSST_CMCC-CM2-VHR4 ()			0.0706 (0.0509 ... 0.0866)	3.789
highresSST_CNRM-CM6-1-HR ()			0.215 (0.153 ... 0.269)	1.907
highresSST_CNRM-CM6-1 ()			0.229 (0.174 ... 0.272)	2.047
highresSST_EC-Earth3P-HR ()			0.109 (0.0818 ... 0.128)	3.093
highresSST_EC-Earth3P ()			0.123 (0.0997 ... 0.142)	2.851
highresSST_HadGEM3-GC31-HM ()			0.112 (0.0748 ... 0.149)	3.589
highresSST_HadGEM3-GC31-LM ()			0.0939 (0.0748 ... 0.107)	3.742
highresSST_HadGEM3-GC31-MM ()			0.0867 (0.0687 ... 0.0981)	3.961
highresSST_MPI-ESM1-2-HR ()			0.113 (0.0832 ... 0.142)	3.137
highresSST_MPI-ESM1-2-XR ()			0.116 (0.0863 ... 0.144)	3.090

*Table 2: Evaluation results for the climate models considered for the attribution analysis of **OND temperature for CSA region**. The table contains qualitative assessments of seasonal cycle and spatial pattern of precipitation from the models (good, reasonable, bad) along with estimates for dispersion parameter and event magnitude. The corresponding estimates for observations are shown in blue. Based on overall suitability, the models are classified as good, reasonable and bad, shown by green, yellow and red highlights, respectively.*

	Temperature			
Observations			Sigma	
CPC			0.493 (0.402 ... 0.555)	
ERA5			0.495 (0.423 ... 0.551)	
Models	**Seasonal cycle**	**Spatial pattern**	**Sigma**	**Threshold for 2-yr return period (°C)**
FLOR historical-rcp4.5 (10)	good	good	0.934 (0.878 ... 0.985)	21.489
AM2.5C360 amipHistorical+rcp4.5SST (3)	good	good	0.908 (0.827 ... 0.985)	22.874
SAM-22_MOHC-HadGEM2-ES_rcp85_r1i1p1_GERICS-REMO2015 ()	good	good	0.566 (0.446 ... 0.643)	21.206
SAM-22_MOHC-HadGEM2-ES_rcp85_r1i1p1_ICTP-RegCM4-7 ()	good	good	0.645 (0.512 ... 0.737)	23.630
SAM-22_MPI-M-MPI-ESM-LR_rcp85_r1i1p1_GERICS-REMO2015 ()	good	good	0.522 (0.404 ... 0.610)	21.907
SAM-22_MPI-M-MPI-ESM-MR_rcp85_r1i1p1_ICTP-RegCM4-7 ()	good	good	0.494 (0.370 ... 0.589)	24.194
SAM-22_NCC-NorESM1-M_rcp85_r1i1p1_GERICS-REMO2015 ()	good	good	0.430 (0.349 ... 0.486)	21.133
SAM-22_NCC-NorESM1-M_rcp85_r1i1p1_ICTP-RegCM4-7 ()	good	good	0.390 (0.288 ... 0.461)	23.304
SAM-44_CCCma-CanESM2_rcp85_r1i1p1_SMHI-RCA4 ()	good	good	0.555 (0.406 ... 0.666)	21.241
SAM-44_CCCma-CanESM2_rcp85_r1i1p1_UCAN-WRF341I ()	good	good	0.539 (0.401 ... 0.645)	20.746
SAM-44_CNRM-CERFACS-CNRM-CM5_rcp85_r1i1p1_SMHI-RCA4 ()	good	good	0.456 (0.363 ... 0.519)	21.844

SAM-44_CSIRO-QCCCE-CSIRO-Mk3-6-0_rcp85_r1i1p1_SMHI-RCA4 ()	good	good	0.665 (0.510 ... 0.778)	21.999
SAM-44_ICHEC-EC-EARTH_rcp85_r12i1p1_SMHI-RCA4 ()	good	good	0.633 (0.485 ... 0.745)	21.607
SAM-44_IPSL-IPSL-CM5A-MR_rcp85_r1i1p1_SMHI-RCA4 ()	good	good	0.773 (0.533 ... 0.960)	23.130
SAM-44_MIROC-MIROC5_rcp85_r1i1p1_SMHI-RCA4 ()	good	good	0.652 (0.500 ... 0.752)	21.670
SAM-44_MOHC-HadGEM2-ES_rcp85_r1i1p1_SMHI-RCA4 ()	good	good	0.691 (0.526 ... 0.805)	21.348
SAM-44_MPI-M-MPI-ESM-LR_rcp85_r1i1p1_MPI-CSC-REMO2009 ()	good	good	0.557 (0.421 ... 0.662)	22.081
SAM-44_MPI-M-MPI-ESM-LR_rcp85_r1i1p1_SMHI-RCA4 ()	good	good	0.566 (0.400 ... 0.699)	22.099
SAM-44_NCC-NorESM1-M_rcp85_r1i1p1_SMHI-RCA4 ()	good	good	0.449 (0.356 ... 0.515)	21.112
SAM-44_NOAA-GFDL-GFDL-ESM2M_rcp85_r1i1p1_SMHI-RCA4 ()	good	good	0.643 (0.478 ... 0.769)	21.923
ACCESS-CM2_r1i1p1f1 ()	bad	good	0.250 (0.190 ... 0.290)	17.69
ACCESS-ESM1-5_r1i1p1f1 ()	good	good	0.490 (0.380 ... 0.560)	21.95
CanESM5_r1i1p1f1 ()	good	good	0.420 (0.330 ... 0.480)	21.56
CMCC-ESM2_r1i1p1f1 ()	good	good	0.520 (0.380 ... 0.630)	22.3
CNRM-CM6-1-HR_r1i1p1f2 ()	good	good	0.710 (0.540 ... 0.840)	21.49
CNRM-CM6-1_r1i1p1f2 ()	good	good	0.690 (0.520 ... 0.810)	20.31
CNRM-ESM2-1_r1i1p1f2 ()	good	good	0.820 (0.580 ... 1.06)	21.03
EC-Earth3_r1i1p1f1 ()	good	good	0.500 (0.380 ... 0.590)	21.32
EC-Earth3-CC_r1i1p1f1 ()	good	good	0.490 (0.370 ... 0.580)	21.32
EC-Earth3-Veg_r1i1p1f1 ()	good	good	0.570 (0.450 ... 0.660)	21.55
EC-Earth3-Veg-LR_r1i1p1f1 ()	good	good	0.570 (0.440 ... 0.660)	21.16
FGOALS-g3_r1i1p1f1 ()	good	good	0.450 (0.370 ... 0.510)	22.61
HadGEM3-GC31-LL_r1i1p1f3 ()	bad	good	0.220 (0.160 ... 0.260)	17.8
HadGEM3-GC31-MM_r1i1p1f3 ()	good	good	0.520 (0.390 ... 0.620)	21.71
INM-CM4-8_r1i1p1f1 ()	good	good	0.690 (0.520 ... 0.780)	22.38

INM-CM5-0_r1i1p1f1 ()	good	good	0.580 (0.440 ... 0.680)	21.98
IPSL-CM6A-LR_r1i1p1f1 ()	good	good	0.630 (0.510 ... 0.720)	22.05
KACE-1-0-G_r1i1p1f1 ()	bad	good	0.180 (0.130 ... 0.230)	18.09
MIROC6_r1i1p1f1 ()	good	good	0.630 (0.490 ... 0.720)	26.24
MPI-ESM1-2-HR_r1i1p1f1 ()	good	good	0.600 (0.410 ... 0.740)	21.48
MPI-ESM1-2-LR_r1i1p1f1 ()	good	good	0.720 (0.560 ... 0.830)	22
MRI-ESM2-0_r1i1p1f1 ()	good	good	0.710 (0.580 ... 0.810)	22.65
NESM3_r1i1p1f1 ()	good	good	0.570 (0.450 ... 0.660)	23.01
NorESM2-LM_r1i1p1f1 ()	good	good	0.620 (0.450 ... 0.730)	23.11
NorESM2-MM_r1i1p1f1 ()	good	good	0.550 (0.400 ... 0.640)	23.11
TaiESM1_r1i1p1f1 ()	good	good	0.470 (0.370 ... 0.530)	21.53
UKESM1-0-LL_r1i1p1f2 ()	bad	good	0.190 (0.140 ... 0.220)	17.31
ukcp-land-gcm_01 ()	reasonable	good	0.592 (0.458 ... 0.701)	22.6
ukcp-land-gcm_02 ()	reasonable	good	0.538 (0.392 ... 0.644)	22.5
ukcp-land-gcm_03 ()	reasonable	good	0.525 (0.383 ... 0.627)	21.8
ukcp-land-gcm_04 ()	reasonable	good	0.589 (0.456 ... 0.677)	22.2
ukcp-land-gcm_05 ()	reasonable	good	0.578 (0.431 ... 0.692)	22.9
ukcp-land-gcm_06 ()	reasonable	good	0.603 (0.460 ... 0.705)	23.0
ukcp-land-gcm_07 ()	reasonable	good	0.468 (0.367 ... 0.537)	22.0
ukcp-land-gcm_08 ()	reasonable	good	0.699 (0.552 ... 0.804)	23.0
ukcp-land-gcm_09 ()	reasonable	good	0.524 (0.395 ... 0.609)	22.6
ukcp-land-gcm_10 ()	reasonable	good	0.510 (0.394 ... 0.617)	22.2
ukcp-land-gcm_11 ()	reasonable	good	0.606 (0.479 ... 0.696)	22.4
ukcp-land-gcm_12 ()	reasonable	good	0.550 (0.430 ... 0.645)	22.3
ukcp-land-gcm_13 ()	reasonable	good	0.531 (0.420 ... 0.606)	22.3
ukcp-land-gcm_14 ()	reasonable	good	0.483 (0.351 ... 0.572)	23.2
ukcp-land-gcm_15 ()	reasonable	good	0.568 (0.424 ... 0.671)	23.0
highresSST_CMCC-CM2-HR4 ()			0.421 (0.333 ... 0.480)	22.426
highresSST_CMCC-CM2-VHR4 ()			0.461 (0.340 ... 0.553)	22.269
highresSST_CNRM-CM6-1-HR ()			0.755 (0.557 ... 0.901)	22.406
highresSST_CNRM-CM6-1 ()			0.936 (0.714 ... 1.13)	21.105

highresSST_EC-Earth3P-HR ()			0.479 (0.366 ... 0.554)	20.818
highresSST_EC-Earth3P ()			0.491 (0.378 ... 0.573)	21.562
highresSST_HadGEM3-GC31-HM ()			0.528 (0.409 ... 0.604)	22.049
highresSST_HadGEM3-GC31-LM ()			0.644 (0.516 ... 0.740)	21.49
highresSST_HadGEM3-GC31-MM ()			0.534 (0.415 ... 0.627)	21.278
highresSST_MPI-ESM1-2-HR ()			0.589 (0.427 ... 0.705)	21.573
highresSST_MPI-ESM1-2-XR ()			0.621 (0.495 ... 0.709)	

5 Multi-method multi-model attribution

This section shows Probability Ratios and change in event intensity ΔI in the climate models, for precipitation (Table 3), temperature (Table 4) and effective precipitation (Table 5) in the CSA region during the 2022 OND season. The tables show the model-based results for the models that are labelled 'reasonable' or 'good'.

*Table 3: Probability ratio and change in intensity in **precipitation** for models that passed the validation tests,*

Model / Observations	a. Past vs. present		b. Present vs. future	
	Probability ratio PR [-]	Change in intensity ΔI [%]	Probability ratio PR [-]	Change in intensity ΔI [%]
CHIRPS	0.59 (0.049 ... 5.6)	6.3 (-17 ... 36)		
CPC	5.1 (0.42 ... 1.4e+2)	-15 (-33 ... 8.2)		
MSWEP	3.4 (0.34 ... 52)	-13 (-34 ... 13)		
FLOR historical-rcp4.5 (10)	0.58 (0.47 ... 0.71)	5.6 (3.6 ... 7.5)	0.51 (0.42 ... 0.63)	3.7 (2.8 ... 4.7)
AM2.5C360 amipHistorical+rcp4.5SST (3)	0.79 (0.38 ... 1.4)	2.2 (-3.0 ... 9.1)	0.87 (0.66 ... 1.1)	1.2 (-0.64 ... 3.7)
SAM-22_MOHC-HadGEM2-ES_rcp85_r1i1p1_ICTP-RegCM4-7 ()	0.62 (0.26 ... 1.8)	4.1 (-4.5 ... 13)	0.78 (0.54 ... 1.1)	1.8 (-0.65 ... 4.3)
SAM-22_MPI-M-MPI-ESM-LR_rcp85_r1i1p1_GERICS-REMO2015 ()	0.37 (0.14 ... 1.4)	9.6 (-2.5 ... 22)	0.42 (0.25 ... 0.69)	6.6 (2.9 ... 10)
SAM-22_MPI-M-MPI-ESM-MR_rcp85_r1i1p1_ICTP-RegCM4-7 ()	0.87 (0.25 ... 3.4)	1.3 (-9.7 ... 14)	0.74 (0.45 ... 1.1)	3.1 (-0.81 ... 7.6)
SAM-22_NCC-NorESM1-M_rcp85_r1i1p1_ICTP-RegCM4-7 ()	0.59 (0.17 ... 3.9)	4.5 (-9.5 ... 19)	0.79 (0.43 ... 1.4)	1.9 (-2.9 ... 5.9)
SAM-44_CSIRO-QCCCE-CSIRO-Mk3-6-0_rcp85_r1i1p1_SMHI-RCA4 ()	0.64 (0.18 ... 3.5)	2.8 (-6.9 ... 12)	0.92 (0.56 ... 1.4)	0.46 (-2.0 ... 3.0)
SAM-44_ICHEC-EC-EARTH_rcp85_r12i1p1_SMHI-RCA4 ()	0.41 (0.15 ... 1.1)	7.2 (-0.95 ... 16)	0.69 (0.49 ... 0.92)	3.1 (0.67 ... 6.0)

SAM-44_MIROC-MIROC5_rcp85_r1i1p1_SMHI-RCA4 ()	0.48 (0.17 ... 1.6)	7.7 (-4.3 ... 22)	0.82 (0.56 ... 1.3)	2.0 (-2.1 ... 5.8)
SAM-44_MOHC-HadGEM2-ES_rcp85_r1i1p1_SMHI-RCA4 ()	0.79 (0.38 ... 1.6)	1.9 (-3.3 ... 7.9)	1.1 (0.80 ... 1.4)	-0.42 (-2.5 ... 1.6)
SAM-44_MPI-M-MPI-ESM-LR_rcp85_r1i1p1_MPI-CSC-REMO2009 ()	0.52 (0.22 ... 1.2)	5.5 (-1.3 ... 14)	0.44 (0.29 ... 0.68)	5.7 (2.9 ... 8.5)
SAM-44_NCC-NorESM1-M_rcp85_r1i1p1_SMHI-RCA4 ()	0.50 (0.17 ... 2.2)	5.6 (-4.9 ... 16)	0.93 (0.56 ... 1.4)	0.53 (-2.4 ... 4.0)
SAM-44_NOAA-GFDL-GFDL-ESM2M_rcp85_r1i1p1_SMHI-RCA4 ()	0.71 (0.25 ... 2.3)	3.1 (-6.3 ... 14)	1.1 (0.72 ... 1.6)	-0.61 (-4.0 ... 2.9)
CNRM-CM6-1-HR_r1i1p1f2 ()	0.98 (0.53 ... 1.9)	0.23 (-5.6 ... 6.4)	0.90 (0.74 ... 1.1)	0.97 (-1.1 ... 2.8)
CNRM-CM6-1_r1i1p1f2 ()	0.60 (0.30 ... 1.1)	6.3 (-0.74 ... 15)	0.82 (0.66 ... 1.0)	2.0 (-0.21 ... 4.3)
CNRM-ESM2-1_r1i1p1f2 ()	0.54 (0.23 ... 1.1)	7.0 (-1.1 ... 16)	0.93 (0.68 ... 1.2)	0.73 (-1.8 ... 3.4)
INM-CM4-8_r1i1p1f1 ()	1.1 (0.21 ... 4.3)	-0.68 (-8.5 ... 8.6)	0.96 (0.62 ... 1.4)	0.26 (-2.0 ... 2.4)
IPSL-CM6A-LR_r1i1p1f1 ()	0.57 (0.24 ... 1.1)	4.6 (-0.61 ... 11)	0.70 (0.52 ... 0.92)	2.5 (0.65 ... 4.2)
MIROC6_r1i1p1f1 ()	0.22 (0.070 ... 0.64)	16 (4.5 ... 31)	0.59 (0.34 ... 0.91)	4.3 (0.81 ... 7.6)
MPI-ESM1-2-LR_r1i1p1f1 ()	0.39 (0.13 ... 1.2)	8.3 (-1.3 ... 17)	0.62 (0.40 ... 0.87)	3.4 (0.98 ... 5.9)
MRI-ESM2-0_r1i1p1f1 ()	0.80 (0.31 ... 2.1)	2.2 (-6.6 ... 11)	0.88 (0.68 ... 1.1)	1.2 (-0.96 ... 3.2)
NorESM2-LM_r1i1p1f1 ()	0.43 (0.15 ... 1.1)	11 (-0.89 ... 27)	0.49 (0.33 ... 0.67)	8.2 (4.6 ... 12)
NorESM2-MM_r1i1p1f1 ()	0.16 (0.040 ... 0.40)	34 (14 ... 64)	0.56 (0.37 ... 0.79)	6.4 (2.7 ... 9.9)
ukcp-land-gcm_01 ()	0.51 (0.25 ... 1.1)	5.2 (-0.57 ... 12)	0.71 (0.52 ... 0.92)	2.5 (0.70 ... 4.4)
ukcp-land-gcm_02 ()	0.81 (0.33 ... 2.4)	1.6 (-5.4 ... 8.9)	0.93 (0.73 ... 1.2)	0.47 (-1.2 ... 1.9)
ukcp-land-gcm_07 ()	0.54 (0.28 ... 1.2)	5.7 (-1.2 ... 13)	0.89 (0.68 ... 1.1)	1.0 (-0.99 ... 2.9)
ukcp-land-gcm_08 ()	0.51 (0.23 ... 1.3)	6.1 (-2.2 ... 15)	0.74 (0.54 ... 0.99)	2.6 (0.11 ... 4.8)
ukcp-land-gcm_12 ()	1.6 (0.46 ... 8.1)	-3.6 (-13 ... 6.8)	0.63 (0.41 ... 0.90)	3.2 (0.76 ... 5.2)
ukcp-land-gcm_14 ()	0.56 (0.25 ... 1.3)	4.3 (-1.7 ... 11)	0.73 (0.56 ... 0.91)	2.1 (0.63 ... 3.5)
highresSST_CNRM-CM6-1-HR ()	0.43 (0.20 ... 0.96)	11 (0.48 ... 24)	0.62 (0.37 ... 0.95)	6.6 (0.62 ... 13)
highresSST_CNRM-CM6-1 ()	0.39 (0.17 ... 0.89)	13 (1.3 ... 26)	0.58 (0.32 ... 0.97)	7.9 (0.37 ... 15)
highresSST_EC-Earth3P-HR ()	0.75 (0.21 ... 4.5)	2.1 (-8.9 ... 14)	0.68 (0.22 ... 1.8)	2.7 (-4.7 ... 8.9)
highresSST_EC-Earth3P ()	0.58 (0.20 ... 2.4)	4.5 (-6.0 ... 15)	0.67 (0.26 ... 1.4)	3.0 (-2.7 ... 8.7)
highresSST_HadGEM3-GC31-HM ()	1.2 (0.31 ... 5.8)	-1.6 (-11 ... 9.8)	1.2 (0.43 ... 2.2)	-1.1 (-7.1 ... 5.0)
highresSST_MPI-ESM1-2-HR ()	2.0 (0.45 ... 17)	-4.4 (-14 ... 5.4)	1.4 (0.52 ... 3.1)	-2.3 (-8.5 ... 3.4)
highresSST_MPI-ESM1-2-XR ()	0.97 (0.27 ... 4.2)	0.24 (-9.5 ... 11)	0.85 (0.34 ... 1.8)	1.3 (-5.3 ... 7.0)

*Table 4: Probability ratio and change in intensity in **temperature** for models that passed the validation tests,*

Model / Observations	a. Past vs. present		b. Present vs. future	
	Probability ratio PR [-]	Change in intensity ΔI [°C]	Probability ratio PR [-]	Change in intensity ΔI [°C]
CPC	24 (3.0 ... 1.1e+3)	1.1 (0.43 ... 1.8)		
ERA5	2.6e+2 (39 ... 4.0e+3)	1.4 (0.97 ... 1.8)		
SAM-22_MOHC-HadGEM2-ES_rcp85_r1i1p1_GERICS-REMO2015 ()	2.8 (1.2 ... 13)	0.53 (0.12 ... 0.94)	1.3 (1.2 ... 1.4)	0.56 (0.46 ... 0.66)

SAM-22_MOHC-HadGEM2-ES_rcp85_r1i1p1_ICTP-RegCM4-7 ()	3.9 (1.5 ... 23)	0.70 (0.28 ... 1.1)	1.5 (1.3 ... 1.6)	0.59 (0.49 ... 0.69)
SAM-22_MPI-M-MPI-ESM-LR_rcp85_r1i1p1_GERICS-REMO2015 ()	5.4 (1.4 ... 71)	0.76 (0.23 ... 1.3)	1.6 (1.5 ... 1.9)	0.58 (0.42 ... 0.76)
SAM-22_NCC-NorESM1-M_rcp85_r1i1p1_GERICS-REMO2015 ()	8.4 (1.4 ... 3.2e+2)	0.72 (0.16 ... 1.2)	1.7 (1.5 ... 2.0)	0.50 (0.37 ... 0.62)
SAM-22_NCC-NorESM1-M_rcp85_r1i1p1_ICTP-RegCM4-7 ()	3.6 (0.96 ... 66)	0.48 (-0.019 ... 0.96)	1.5 (1.3 ... 1.6)	0.53 (0.39 ... 0.67)
SAM-44_CCCma-CanESM2_rcp85_r1i1p1_SMHI-RCA4 ()	17 (5.8 ... 1.2e+2)	0.99 (0.74 ... 1.3)	1.6 (1.4 ... 1.8)	0.75 (0.66 ... 0.83)
SAM-44_CCCma-CanESM2_rcp85_r1i1p1_UCAN-WRF341I ()	7.0 (3.0 ... 28)	0.75 (0.50 ... 1.0)	1.4 (1.3 ... 1.6)	0.65 (0.57 ... 0.73)
SAM-44_CNRM-CERFACS-CNRM-CM5_rcp85_r1i1p1_SMHI-RCA4 ()	46 (7.0 ... 1.1e+3)	1.1 (0.72 ... 1.6)	1.9 (1.6 ... 2.2)	0.78 (0.63 ... 0.92)
SAM-44_CSIRO-QCCCE-CSIRO-Mk3-6-0_rcp85_r1i1p1_SMHI-RCA4 ()	29 (4.1 ... 1.2e+3)	1.3 (0.70 ... 2.1)	1.7 (1.5 ... 2.0)	0.98 (0.82 ... 1.2)
SAM-44_ICHEC-EC-EARTH_rcp85_r12i1p1_SMHI-RCA4 ()	17 (3.3 ... 3.2e+2)	1.2 (0.67 ... 1.7)	1.7 (1.6 ... 2.0)	0.86 (0.71 ... 0.99)
SAM-44_IPSL-IPSL-CM5A-MR_rcp85_r1i1p1_SMHI-RCA4 ()	61 (9.2 ... 2.3e+3)	1.7 (1.3 ... 2.2)	1.9 (1.7 ... 2.3)	1.1 (0.97 ... 1.3)
SAM-44_MIROC-MIROC5_rcp85_r1i1p1_SMHI-RCA4 ()	8.3 (2.2 ... 91)	1.1 (0.54 ... 1.5)	1.6 (1.4 ... 1.8)	0.82 (0.64 ... 1.0)
SAM-44_MOHC-HadGEM2-ES_rcp85_r1i1p1_SMHI-RCA4 ()	5.4 (2.5 ... 23)	0.83 (0.51 ... 1.2)	1.4 (1.3 ... 1.5)	0.72 (0.64 ... 0.81)
SAM-44_MPI-M-MPI-ESM-LR_rcp85_r1i1p1_MPI-CSC-REMO2009 ()	5.8 (2.2 ... 32)	0.81 (0.44 ... 1.1)	1.6 (1.5 ... 1.8)	0.58 (0.44 ... 0.71)
SAM-44_MPI-M-MPI-ESM-LR_rcp85_r1i1p1_SMHI-RCA4 ()	8.4 (2.7 ... 72)	0.87 (0.55 ... 1.2)	1.6 (1.4 ... 1.8)	0.67 (0.54 ... 0.79)
SAM-44_NCC-NorESM1-M_rcp85_r1i1p1_SMHI-RCA4 ()	23 (3.5 ... 4.8e+2)	0.98 (0.53 ... 1.4)	1.7 (1.5 ... 1.9)	0.72 (0.60 ... 0.85)
SAM-44_NOAA-GFDL-GFDL-ESM2M_rcp85_r1i1p1_SMHI-RCA4 ()	4.6 (1.5 ... 24)	0.85 (0.31 ... 1.3)	1.5 (1.4 ... 1.7)	0.84 (0.64 ... 1.0)
ACCESS-ESM1-5_r1i1p1f1 ()	10 (4.9 ... 24)	0.90 (0.61 ... 1.2)	1.8 (1.6 ... 2.0)	0.65 (0.56 ... 0.73)
CanESM5_r1i1p1f1 ()	1.2e+2 (49 ... 5.4e+2)	1.3 (1.1 ... 1.5)	1.9 (1.6 ... 2.3)	0.87 (0.78 ... 0.95)
CMCC-ESM2_r1i1p1f1 ()	2.4 (1.3 ... 4.8)	0.47 (0.16 ... 0.78)	1.7 (1.6 ... 1.9)	0.63 (0.49 ... 0.77)
CNRM-CM6-1-HR_r1i1p1f2 ()	7.4 (3.9 ... 16)	1.1 (0.75 ... 1.5)	1.7 (1.6 ... 1.9)	0.82 (0.71 ... 0.94)
CNRM-CM6-1_r1i1p1f2 ()	3.8 (2.2 ... 7.2)	0.78 (0.41 ... 1.1)	1.6 (1.5 ... 1.8)	0.69 (0.54 ... 0.82)
EC-Earth3_r1i1p1f1 ()	3.7 (2.3 ... 6.5)	0.60 (0.38 ... 0.82)	1.6 (1.5 ... 1.8)	0.45 (0.37 ... 0.53)
EC-Earth3-CC_r1i1p1f1 ()	2.6 (1.7 ... 4.4)	0.48 (0.25 ... 0.69)	1.6 (1.5 ... 1.8)	0.51 (0.40 ... 0.62)
EC-Earth3-Veg_r1i1p1f1 ()	11 (6.2 ... 22)	0.91 (0.63 ... 1.2)	1.7 (1.6 ... 2.0)	0.60 (0.51 ... 0.68)
EC-Earth3-Veg-LR_r1i1p1f1 ()	5.5 (2.5 ... 13)	0.84 (0.47 ... 1.2)	1.7 (1.6 ... 1.9)	0.70 (0.56 ... 0.83)
FGOALS-g3_r1i1p1f1 ()	13 (7.2 ... 27)	0.81 (0.57 ... 1.0)	1.8 (1.6 ... 2.1)	0.63 (0.55 ... 0.73)
HadGEM3-GC31-MM_r1i1p1f3 ()	31 (13 ... 1.1e+2)	1.1 (0.82 ... 1.4)	1.9 (1.7 ... 2.1)	0.76 (0.68 ... 0.83)
INM-CM4-8_r1i1p1f1 ()	19 (5.7 ... 68)	1.3 (0.67 ... 1.8)	1.9 (1.6 ... 2.2)	1.0 (0.85 ... 1.2)

Model / Observations	Probability ratio PR [-]	Change in intensity ΔI [mm/day]	Probability ratio PR [-]	Change in intensity ΔI [mm/day]
INM-CM5-0_r1i1p1f1 ()	3.9 (1.7 ... 10)	0.69 (0.25 ... 1.1)	1.8 (1.6 ... 2.1)	0.83 (0.67 ... 0.97)
IPSL-CM6A-LR_r1i1p1f1 ()	5.2 (2.8 ... 11)	0.90 (0.54 ... 1.3)	1.8 (1.6 ... 2.0)	0.79 (0.67 ... 0.91)
MIROC6_r1i1p1f1 ()	3.5 (1.5 ... 9.3)	0.80 (0.28 ... 1.3)	1.7 (1.6 ... 1.9)	0.80 (0.61 ... 0.99)
MPI-ESM1-2-HR_r1i1p1f1 ()	30 (13 ... 95)	1.3 (1.0 ... 1.7)	1.8 (1.6 ... 2.0)	0.83 (0.68 ... 0.99)
NESM3_r1i1p1f1 ()	18 (9.8 ... 40)	1.2 (0.97 ... 1.6)	1.9 (1.6 ... 2.2)	1.0 (0.90 ... 1.1)
NorESM2-LM_r1i1p1f1 ()	0.70 (0.40 ... 1.2)	-0.28 (-0.69 ... 0.16)	1.2 (0.94 ... 1.3)	0.14 (-0.050 ... 0.31)
NorESM2-MM_r1i1p1f1 ()	1.3 (0.70 ... 2.7)	0.16 (-0.24 ... 0.59)	1.6 (1.5 ... 1.7)	0.50 (0.32 ... 0.68)
TaiESM1_r1i1p1f1 ()	2.2e+2 (62 ... 1.4e+3)	1.3 (0.96 ... 1.6)	1.9 (1.7 ... 2.3)	0.82 (0.74 ... 0.90)
ukcp-land-gcm_01 ()	22 (9.0 ... 86)	1.2 (0.94 ... 1.5)	1.9 (1.7 ... 2.2)	0.76 (0.69 ... 0.83)
ukcp-land-gcm_02 ()	1.1e+2 (29 ... 7.5e+2)	1.5 (1.3 ... 1.8)	2.5 (2.2 ... 3.1)	0.86 (0.77 ... 0.97)
ukcp-land-gcm_03 ()	35 (12 ... 1.7e+2)	1.2 (0.98 ... 1.4)	1.8 (1.6 ... 2.1)	0.83 (0.76 ... 0.89)
ukcp-land-gcm_04 ()	23 (6.5 ... 1.3e+2)	1.0 (0.75 ... 1.3)	1.8 (1.6 ... 2.1)	0.69 (0.62 ... 0.77)
ukcp-land-gcm_05 ()	34 (7.9 ... 2.3e+2)	1.3 (0.88 ... 1.5)	2.1 (1.9 ... 2.5)	0.74 (0.65 ... 0.83)
ukcp-land-gcm_06 ()	23 (7.4 ... 1.4e+2)	1.2 (0.83 ... 1.5)	2.0 (1.8 ... 2.4)	0.71 (0.62 ... 0.80)
ukcp-land-gcm_07 ()	88 (17 ... 1.0e+3)	1.3 (1.0 ... 1.6)	2.1 (1.8 ... 2.5)	0.80 (0.71 ... 0.90)
ukcp-land-gcm_08 ()	16 (3.5 ... 2.2e+2)	1.1 (0.65 ... 1.7)	1.7 (1.6 ... 2.0)	0.78 (0.68 ... 0.88)
ukcp-land-gcm_09 ()	1.4e+2 (30 ... 1.8e+3)	1.3 (1.1 ... 1.6)	2.2 (1.9 ... 2.7)	0.83 (0.77 ... 0.90)
ukcp-land-gcm_10 ()	1.3e+2 (32 ... 1.2e+3)	1.4 (1.1 ... 1.7)	2.2 (1.9 ... 2.6)	0.87 (0.79 ... 0.94)
ukcp-land-gcm_11 ()	28 (8.9 ... 1.6e+2)	1.2 (0.94 ... 1.6)	1.7 (1.5 ... 1.9)	0.89 (0.80 ... 0.97)
ukcp-land-gcm_12 ()	7.5 (2.3 ... 45)	0.79 (0.40 ... 1.2)	1.4 (1.3 ... 1.6)	0.75 (0.62 ... 0.89)
ukcp-land-gcm_13 ()	9.7 (3.9 ... 32)	0.90 (0.62 ... 1.2)	1.5 (1.4 ... 1.7)	0.70 (0.61 ... 0.78)
ukcp-land-gcm_14 ()	1.4e+3 (1.5e+2 ... 3.7e+4)	1.6 (1.4 ... 1.9)	3.2 (2.6 ... 4.1)	0.93 (0.86 ... 0.99)
ukcp-land-gcm_15 ()	44 (13 ... 3.2e+2)	1.4 (1.1 ... 1.7)	2.1 (1.8 ... 2.4)	0.90 (0.82 ... 0.98)
highresSST_CMCC-CM2-HR4 ()	3.3e+2 (28 ... 5.2e+4)	1.3 (0.88 ... 1.6)	2.0 (1.5 ... 2.7)	0.81 (0.61 ... 1.0)
highresSST_CMCC-CM2-VHR4 ()	83 (8.3 ... 4.6e+3)	1.0 (0.67 ... 1.3)	1.7 (1.3 ... 2.2)	0.77 (0.57 ... 0.95)
highresSST_EC-Earth3P-HR ()	9.4 (2.3 ... 1.3e+2)	0.76 (0.36 ... 1.2)	1.6 (1.3 ... 1.9)	0.60 (0.34 ... 0.85)
highresSST_EC-Earth3P ()	47 (6.3 ... 2.0e+3)	1.2 (0.77 ... 1.6)	1.7 (1.4 ... 2.1)	0.90 (0.63 ... 1.2)
highresSST_HadGEM3-GC31-HM ()	71 (7.5 ... 6.3e+3)	1.3 (0.77 ... 1.8)	1.8 (1.3 ... 2.3)	0.91 (0.59 ... 1.2)
highresSST_HadGEM3-GC31-LM ()	14 (2.7 ... 3.0e+2)	1.1 (0.53 ... 1.6)	1.7 (1.3 ... 2.0)	0.78 (0.45 ... 1.1)
highresSST_HadGEM3-GC31-MM ()	28 (4.5 ... 6.9e+2)	0.97 (0.56 ... 1.4)	1.5 (1.2 ... 2.0)	0.84 (0.55 ... 1.1)
highresSST_MPI-ESM1-2-HR ()	75 (13 ... 2.5e+3)	1.4 (0.93 ... 1.9)	1.8 (1.4 ... 2.3)	0.98 (0.73 ... 1.2)
highresSST_MPI-ESM1-2-XR ()	7.9 (1.7 ... 1.2e+2)	0.87 (0.31 ... 1.4)	1.6 (1.3 ... 1.8)	0.72 (0.39 ... 1.0)

*Table 5: Probability ratio and change in intensity in **effective precipitation** for models that passed the validation tests,*

Model / Observations	Probability ratio PR [-]	Change in intensity ΔI [mm/day]	Probability ratio PR [-]	Change in intensity ΔI [mm/day]
CNRM-CM6-1-HR_r1i1p1f2 ()	1.1 (0.36 ... 2.8)	-0.010 (-0.18 ... 0.15)	0.80 (0.50 ... 1.1)	0.040 (-0.020 ... 0.10)

Model				
CNRM-CM6-1_r1i1p1f2 ()	0.35 (0.11 ... 0.83)	0.29 (0.060 ... 0.54)	0.68 (0.39 ... 0.96)	0.090 (0.010 ... 0.19)
INM-CM4-8_r1i1p1f1 ()	0.55 (0.080 ... 2.0)	0.060 (-0.070 ... 0.21)	0.95 (0.55 ... 1.4)	0.010 (-0.030 ... 0.050)
IPSL-CM6A-LR_r1i1p1f1 ()	0.57 (0.20 ... 1.4)	0.10 (-0.060 ... 0.26)	0.53 (0.30 ... 0.79)	0.11 (0.050 ... 0.16)
MIROC6_r1i1p1f1 ()	0.17 (0.030 ... 0.67)	0.42 (0.10 ... 0.79)	0.43 (0.15 ... 0.86)	0.16 (0.030 ... 0.28)
NorESM2-LM_r1i1p1f1 ()	0.59 (0.080 ... 2.2)	0.13 (-0.21 ... 0.51)	0.49 (0.21 ... 0.96)	0.17 (0.010 ... 0.33)
NorESM2-MM_r1i1p1f1 ()	0.20 (0.030 ... 0.75)	0.50 (0.090 ... 0.97)	0.58 (0.27 ... 1.0)	0.14 (0.0 ... 0.28)
SAM-44_CSIRO-QCCCE-CSIRO-Mk3-6-0_rcp85_r1i1p1_SMHI-RCA4 ()	1.9 (0.31 ... 37)	-0.18 (-0.85 ... 0.36)	1.8 (1.1 ... 2.7)	-0.18 (-0.34 ... -0.028)
SAM-44_ICHEC-EC-EARTH_rcp85_r12i1p1_SMHI-RCA4 ()	0.51 (0.15 ... 3.1)	0.19 (-0.25 ... 0.63)	1.0 (0.60 ... 1.5)	-0.0082 (-0.14 ... 0.14)
SAM-44_IPSL-IPSL-CM5A-MR_rcp85_r1i1p1_SMHI-RCA4 ()	7.8 (1.7 ... 76)	-0.45 (-0.76 ... -0.13)	2.2 (1.6 ... 3.3)	-0.25 (-0.38 ... -0.13)
SAM-44_MIROC-MIROC5_rcp85_r1i1p1_SMHI-RCA4 ()	0.72 (0.18 ... 4.6)	0.15 (-0.57 ... 0.92)	1.1 (0.63 ... 1.8)	-0.055 (-0.32 ... 0.19)
SAM-44_MOHC-HadGEM2-ES_rcp85_r1i1p1_SMHI-RCA4 ()	1.0 (0.40 ... 3.6)	-0.013 (-0.38 ... 0.32)	1.5 (1.1 ... 2.0)	-0.15 (-0.27 ... -0.043)
SAM-44_NCC-NorESM1-M_rcp85_r1i1p1_SMHI-RCA4 ()	0.56 (0.16 ... 3.6)	0.23 (-0.39 ... 0.86)	1.3 (0.74 ... 2.0)	-0.11 (-0.31 ... 0.11)
SAM-44_NOAA-GFDL-GFDL-ESM2M_rcp85_r1i1p1_SMHI-RCA4 ()	0.84 (0.22 ... 5.8)	0.058 (-0.44 ... 0.60)	1.6 (1.0 ... 2.5)	-0.18 (-0.34 ... -0.0091)

6 Hazard synthesis

In order to identify whether anthropogenic climate change did causally contribute to the low rainfall as well as the low water availability, we calculate the probability ratio as well as the change in intensity using observations and climate models for the region and time period defined above in rainfall as well as effective precipitation. Models which do not pass the validation tests described above are excluded from the analysis. The aim is to synthesise results from models that pass the evaluation along with the observations-based products, to give an overarching attribution statement. **Figs.** 7 and 9 show the changes in probability and intensity for the observations (blue) and models (red) for precipitation for models (red) only in the case of effective precipitation. The figures show results of combining observations and models into a synthesised assessment, following Philip et al., (2020). See also Li and Otto (2022) for more detail.

In this synthesis, we first add a representation error (in quadrature) to the observations, to account for the difference between observations-based datasets that cannot be explained by natural variability. This is shown in these figures as white boxes around the light blue bars. The dark blue bar shows the average over the observation-based products. Next, a term to account for intermodel spread is added (in quadrature) to the natural variability of the models. This is shown in the figures (primarily for intensity changes) as white boxes around the light red bars. The dark red bar shows the model average, consisting of a weighted mean using the (uncorrelated) uncertainties due to natural variability

Observation-based products and models are combined into a single result in two ways. Firstly, we neglect common model uncertainties beyond the intermodel spread that is depicted by the model

average, and compute the weighted average of models (dark red bar) and observations (dark blue bar): this is indicated by the magenta bar. As, due to common model uncertainties, model uncertainty can be larger than the intermodel spread, secondly, we also show the more conservative estimate of an unweighted, direct average of observations (dark red bar) and models (dark blue bar) contributing 50% each, indicated by the white box around the magenta bar in the synthesis figures.
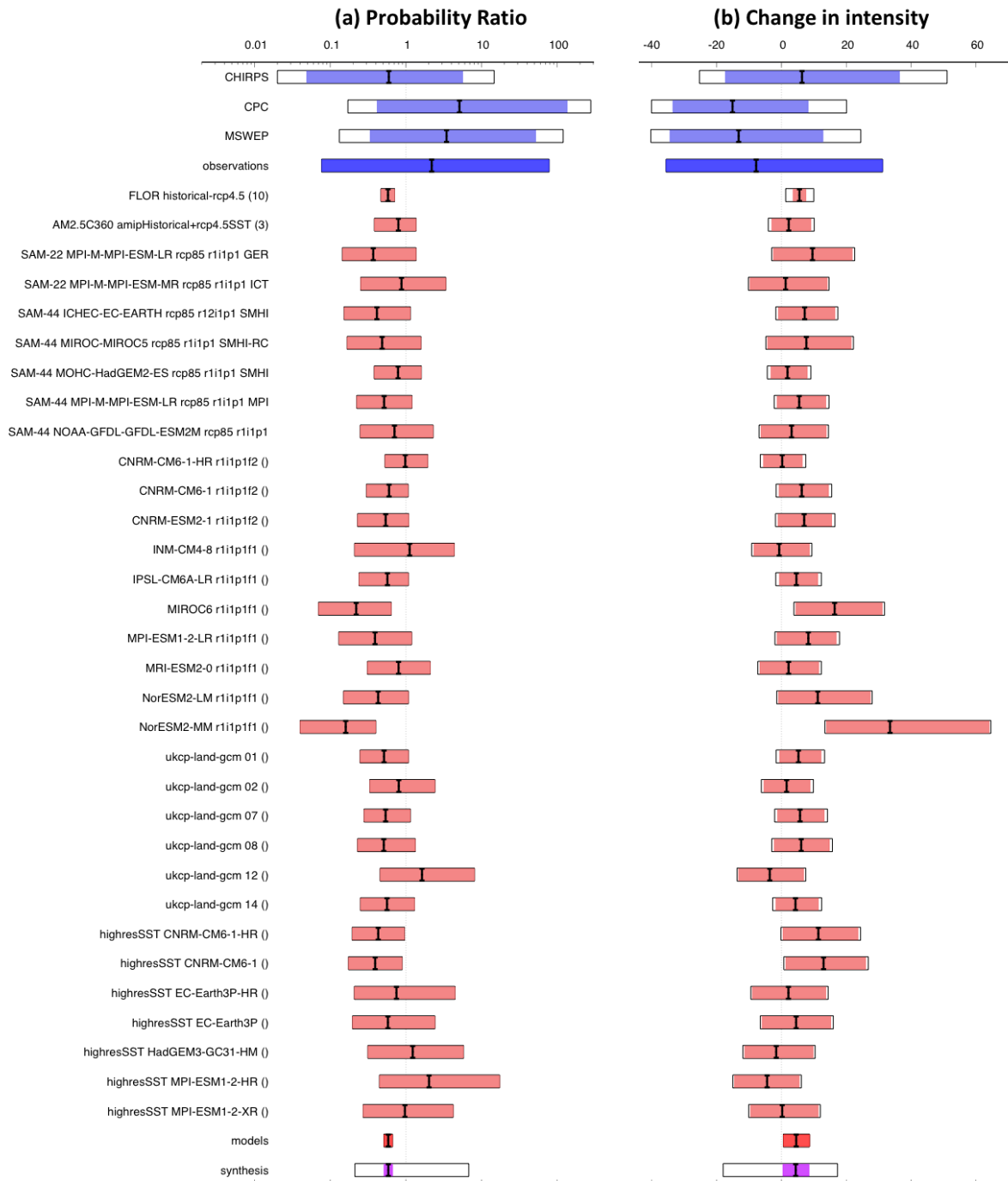

Figure 7: Synthesis of (a) probability ratios and (b) intensity changes when comparing the return period and magnitudes of the 2022 OND precipitation in the current climate and a 1.2ºC cooler climate.
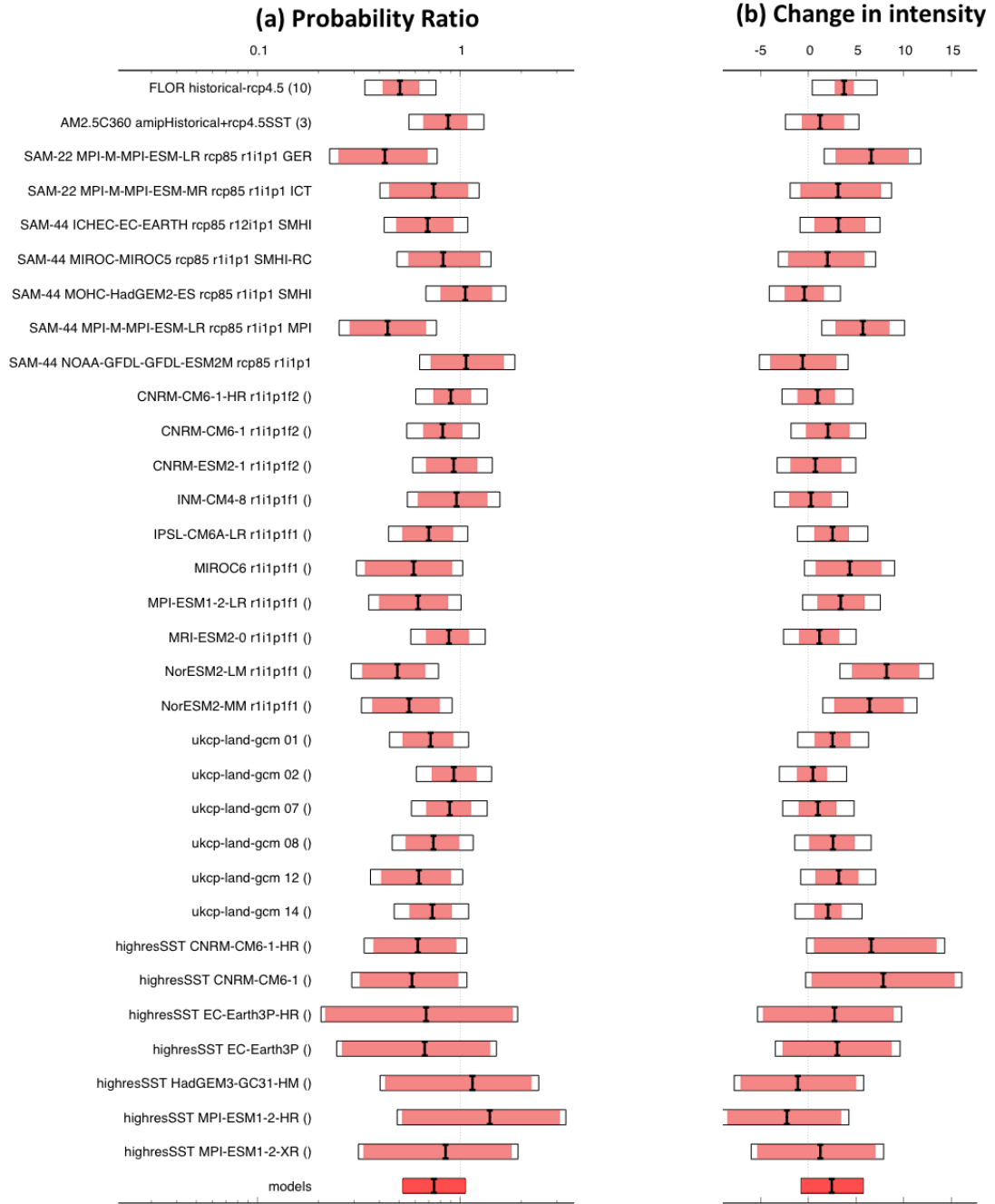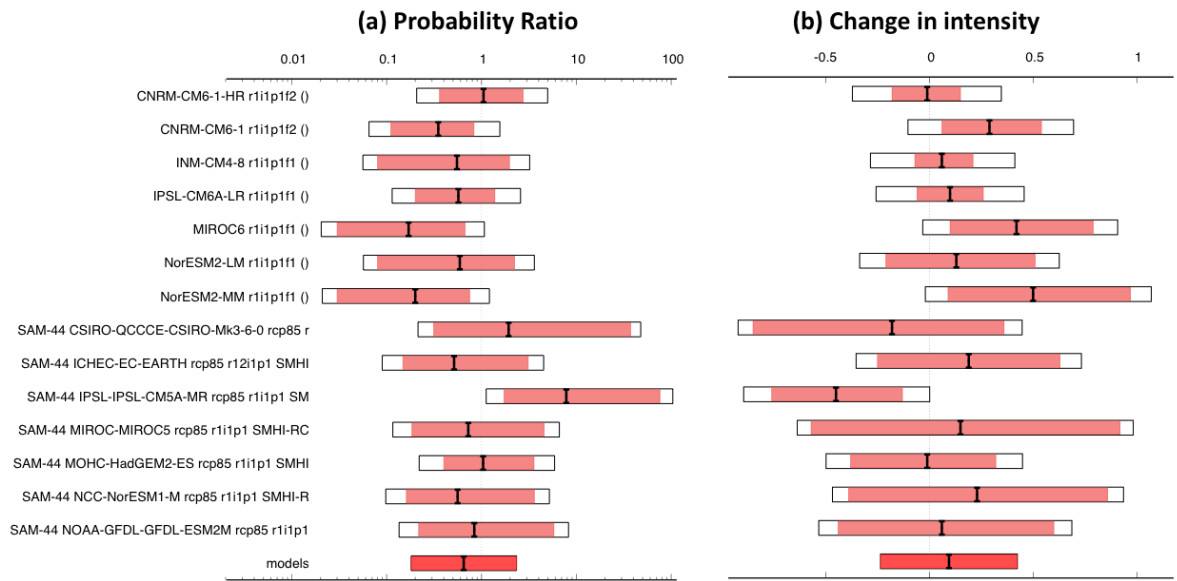
Figure 8: Synthesis of (a) probability ratios and (b) intensity changes when comparing the return period and magnitudes of the 2022 OND precipitation in the current climate and a future 0.8ºC warmer climate.

In the results shown here for precipitation (Fig. 7), the models show a wetting trend that is not significant in many individual models, but only when models are combined (dark red bar). The observations do not show a significant trend, or change in intensity and probability, when combining the three data products there is a small and not significant increase in the probability and intensity of drought.

When looking at effective precipitation, for which we have no observations, we see mostly insignificant changes in both directions, depending on the model, but no trend is emerging. Thus, while there is a wettening in the models when looking at precipitation alone, this is not present when looking at effective precipitation. This could mean that while anthropogenic climate change does lead

to an increase in rainfall and thus a decrease in drought, this is counteracted by the increase in temperature, and thus how much water actually would reach the ground, as seen by the lack of any trend in effective precipitation. This is corroborated when looking at the same event definition but instead of in a 1.2C colder climate, in a 0.8C warmer climate (Figs. 8 & 10). There, we do see a further wetting in the precipitation (dark red bars in Fig. 8) but not when looking at effective precipitation (Fig. 10).

When looking at the change in temperature for the same region and season we do see a clear increase in the likelihood of such a temperature event to occur by a factor of 20 [2.6-180] (Fig. 11, left hand side) and an increase in intensity by approx 1ºC.

Figure 9: Synthesis of (a) probability ratios and (b) intensity changes when comparing the return period and magnitudes of the 2022 OND effective precipitation in the current climate and a 1.2ºC cooler climate.
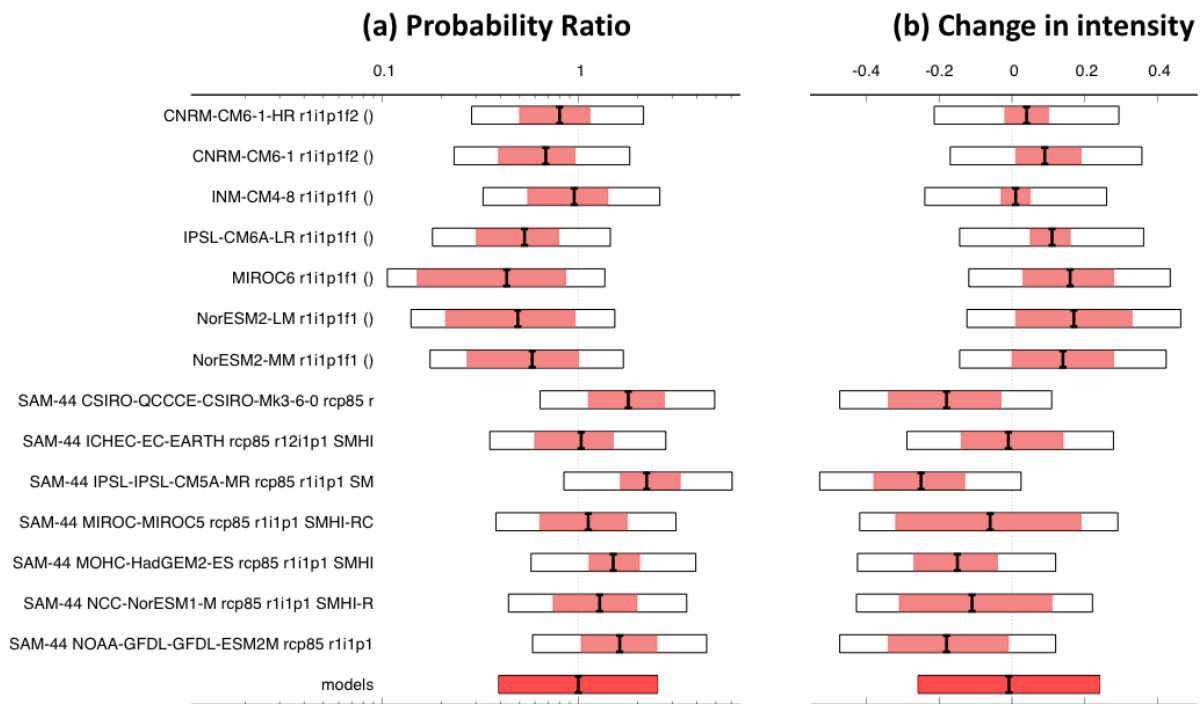
Figure 10: Synthesis of (a) probability ratios and (b) intensity changes when comparing the return period and magnitudes of the 2022 OND effective precipitation in the current climate and a future 0.8°C warmer climate.
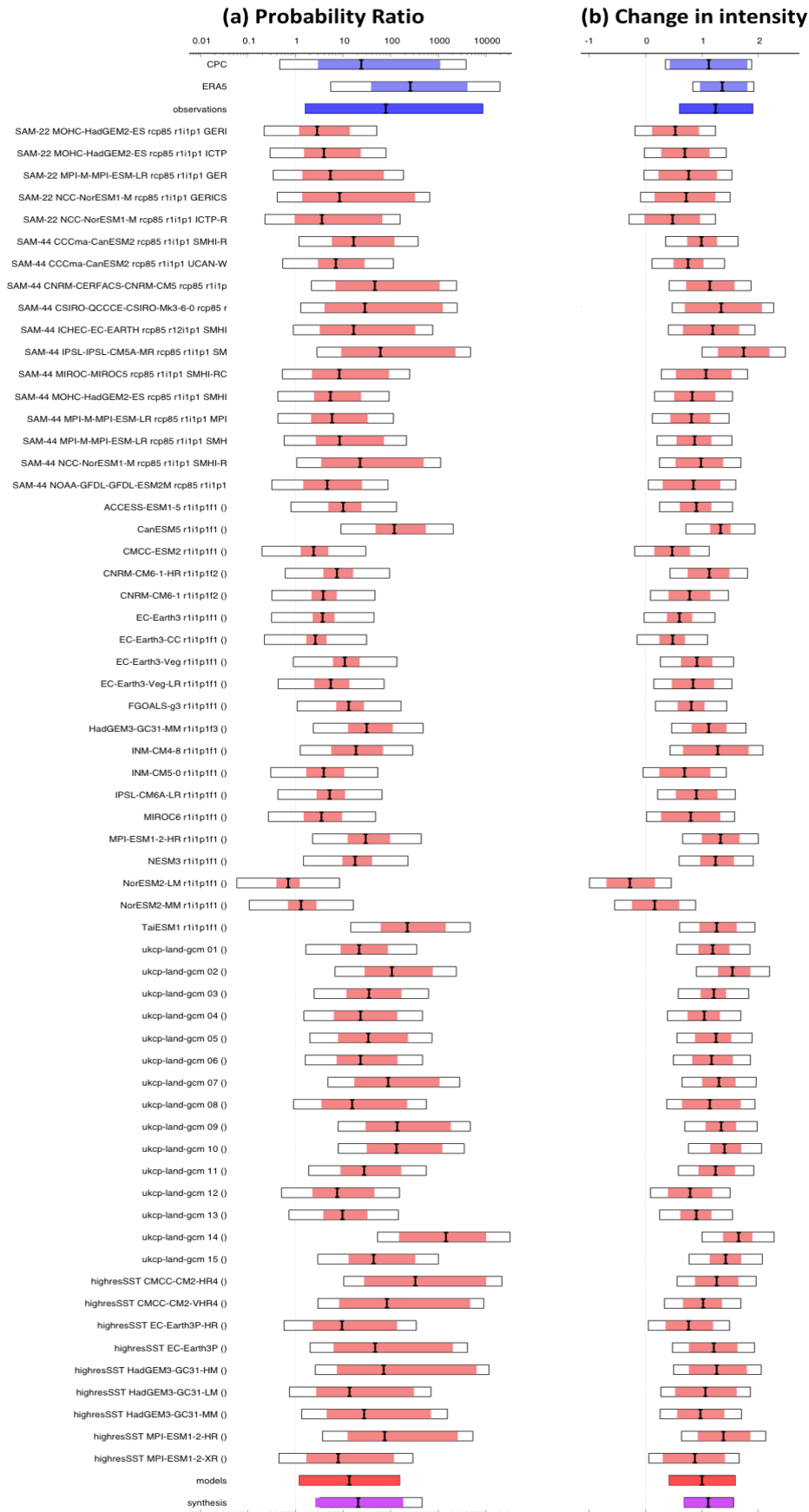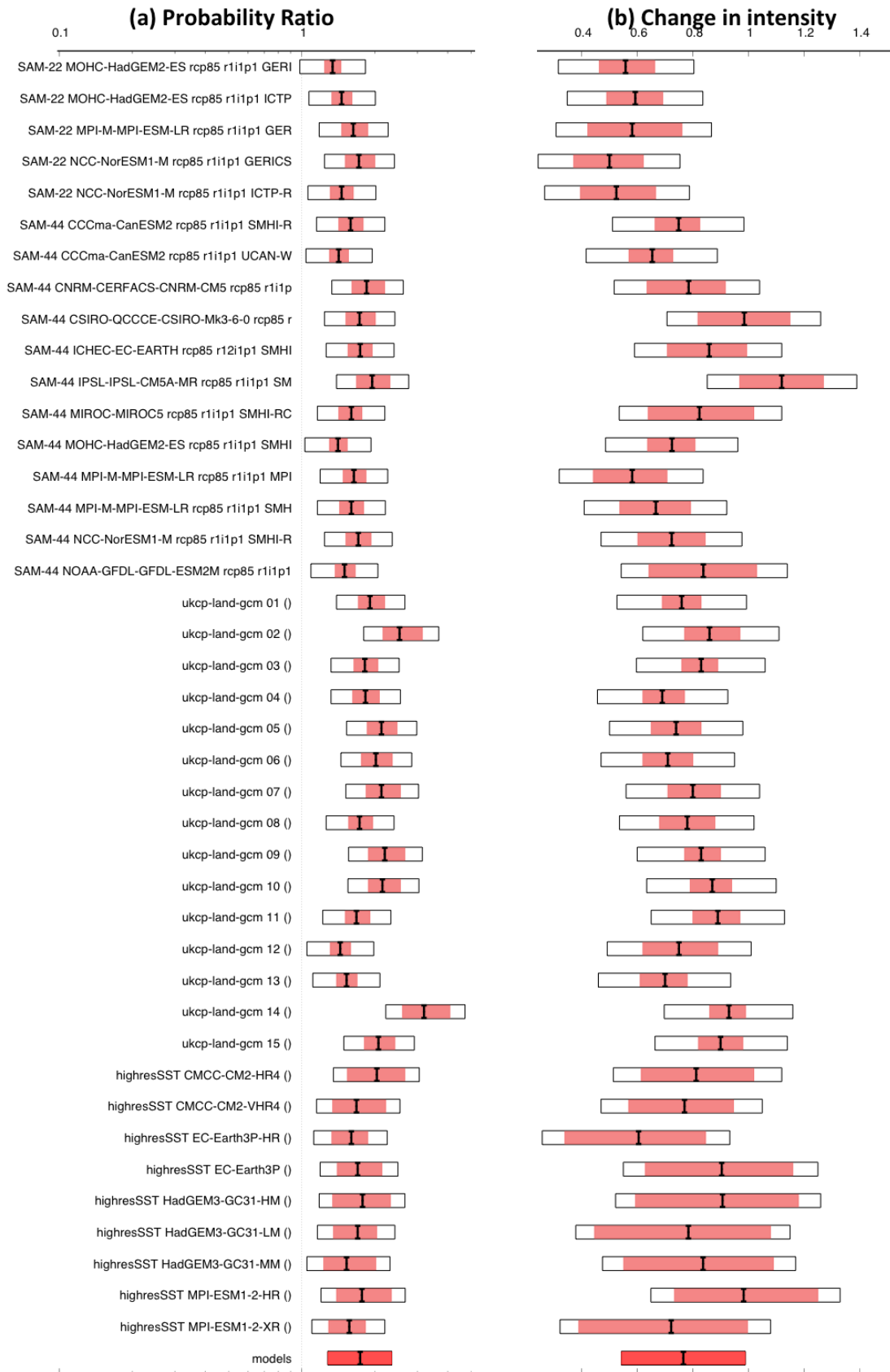
Figure 11: Synthesis of (a) probability ratios and (b) intensity changes when comparing the return period and magnitudes of the 2022 OND temperature in the current climate and a 1.2ºC cooler climate.

Figure 12: Synthesis of (a) probability ratios and (b) intensity changes when comparing the return period and magnitudes of the 2022 OND temperature in the current climate and a future 0.8ºC warmer climate.

Combining all these lines of evidence from the synthesis results of the past climate, results from future projections, the differences in effective precipitation, precipitation and temperature, we conclude that the drought itself, represented as low rainfall, cannot be attributed to anthropogenic climate change, but that the anthropogenic trend in temperature increase the impact of the drought. We do not quantify the increase of the impacts of the drought due to increased temperatures.

7 Vulnerability and exposure

The direct impacts of the meteorological event, lack of rainfall and higher temperatures, combined with vulnerability and exposure factors to create impacts including for farmers whose crop yields were diminished, city-dwellers whose water access was reduced, and people who rely on maritime shipping. In Argentina, vulnerability to drought is concentrated in the north, largely stemming from inadequate infrastructure and comparatively slow social progress, with the highest rates of water scarcity (Naumann et al., 2019; Climate Change Knowledge Portal, 2021). The north is also where most people reside, with half of the population living in the highly urbanised country's ten largest cities, including the metropolitan cities of Buenos Aires (home to one-third), Córdoba, and Rosario (Worldometers, 2023).

The majority of people who are lacking access to the public water supply in Argentina live in those urban centres, and 36 percent are living in poverty (World Bank, 2021). Outside of Argentina's poor urban dwellers, lack of access to public service systems and infrastructure, along with insufficient territorial autonomy, make indigenous peoples another vulnerable group (Hagen et al., 2022). Because the responsibility to collect and carry water mainly tends to fall on women and girls, drought also disproportionately affects them by further limiting time available to spend on education and income-generating activities, which perpetuates gender inequities (World Bank, 2021). Argentina's gaps in access to water supply and sanitation impact the wellbeing of its people and the economy with the average annual economic impact estimated to 1.3 percent of GDP, including losses to quality of life equivalent to US$4.4 billion every year (World Bank, 2021).

7.1 Agriculture impacts and management

The record-breaking heatwaves hitting northern Argentina since November 2022 have significantly aggravated the protracted drought in Central South America, now culminating with the driest conditions and worst crop health in 35 and 40 years, respectively (Rivera et al., 2022; The Western Producer, 2023; World Grain, 2022). The government of Argentina declared a State of Water Emergency for the Paraná basin in July 2021, and the government of Uruguay an agricultural emergency in October 2022 (which was extended in time and scope in January 2023), and the subsequent deterioration is impacting already vulnerable farmers and residents in the agricultural heartland of the continent (Pagina 12, 2023; Prensa Latina, 2022; Mongabay, 2022). In Argentina, this action postpones state and federal taxes, extends loan repayment due dates, and provides immunity against bank foreclosures, which can help farmers struggling with low yields (Bert et al., 2021).

Argentina's wheat production for 2022-23 is projected to be nearly half of the 2021-22 harvest, a drop from 22.4 to 12.4 million tonnes, which equals a 7-year low (Successful Farming, 2023; Colussi, Schnitkey and Paulson, 2022). Similarly, its soybean production is estimated to hit a 5-year low (Gro

Intelligence, 2022; GCaptain, 2023). Argentina moreover saw a 61 percent decrease in grain and oilseed export revenue between January 2023 and 2022 (GCaptain, 2023). As a world-leading soybean and wheat producer and exporter, this decline is a key factor that leads the country's Economy Minister to expect a drought-related US$10 billion loss and 2.2 point reduction in GDP (Buenos Aires Times, 2023). These impacts unfold at a time of sharp devaluation of the Argentine peso, the country's highest annual inflation rate in more than 30 years, and the COVID-19 pandemic which caused significant income losses (BBC, 2023; Bloomberg, 2023; World Bank, 2021). In late January 2023, the government announced its plan to launch a set of support measures to agricultural producers affected by the drought, notably including access to a relief fund totaling roughly US$27 million (Successful Farming, 2023). In order to reduce the financial burden on grain producers, the central bank in Argentina is expected to ease rules on repaying loans, and have more flexible terms on non-payment and subsidised credit lines (The Pig Site, 2023).

However, this is not the first time drought has impacted agricultural production in this region, drought and flood are rather chronic issues in the region. In 2017-18, a drought in the Argentina Pampas was also found to be driven in part due to La Niña conditions, and higher temperatures (Bert et al., 2021). Bert et al. (2021) found that barriers to proactive drought management included limited associations between drought characteristics and the types and magnitude of potential impacts on relevant sectors, as well as lack of clarity on which Argentine institutions should do what and when before, during and after the drought. The knowledge gaps and lack of coordination can be rectified and combined with other government actions such as initiating improved agronomic practices and weather-based insurance schemes, as well as individual level responses such as modifying land allocation or stocking rates to build resilience to drought events (Bert et al., 2021).

7.2 Water management and policy

While home to more than one-third of the world's renewable water resources, water scarcity, inaccessibility, inequality, and pollution remain significant threats to the half a billion people residing across Central and South America (Hagen et al., 2022; Rodríguez et al., 2022). In 2015, only 54 percent of Argentina's rural population and 87 percent of its urban dwellers were connected to the public drinking water supply, totaling up to 8.2 million people (OECD, 2019; World Water Week, n.d.). Shocks such as droughts further exacerbate this water insecurity. Shortly after the drought onset in 2019, farmers around Buenos Aires have suffered from water shortages while thousands of cattle have perished (Gizmodo, 2023; Reuters, 2022; Pagina12, 2023). In July 2021, the Argentine government declared a State of Water Emergency due to the deteriorating situation in the Paraná basin, which was then affecting 40 million people throughout Argentina, Paraguay, and Brazil (Pagina12, 2023; Mongabay, 2022). The Paraná River was at historical lows in the last three years, impacting ecosystems, hydroelectric energy production, and critical transport of goods such as soy and grain (Reuters, 2021). At the time of writing, over 75.000 people in Uruguay cannot access safe drinking water, and access to water for crops and livestock remains limited, despite the country's unparallelled access to safe, quality drinking water among Latin American countries (IFRC, 2023; Euroclima, 2022; Borgen Magazine, 2017).

In order to improve the management of hydroelectricity supply during drought periods, Argentina's second-largest energy source, researchers have suggested integrating remote sensing, modelling, and monitoring data to evaluate droughts and understand how the meteorological event leads to hydrological impacts that can be used to anticipate and manage future impacts (Melo et al., 2016; World Bank, 2021). Addressing hydroelectricity risks is moreover one of the key themes in

Argentina's US$44 billion *National Water Plan* launched in 2016, which centres on ensuring universal access to clean drinking water and adapting to extreme weather events by 2030 (BNamericas, 2017; IWA Network, 2017). By 2021, Argentina had implemented key measures to minimise the water gap, including increasing sanitation and water services to the most vulnerable, reinforced tools such as the National Water Network Information System (SNIH), and created new agencies such as the National Directorate of Drinking Water and Sanitation (DNAPyS) (World Bank, 2021). These measures could help to reduce the impacts of droughts such as this one.

7.3 Vulnerability and exposure conclusion

The heatwave-fuelled drought across Central South America has brought far-reaching impacts to the agricultural and water sectors in Argentina and Uruguay, significantly affecting both human health and the economy. Scaling up financial support and insurance instruments available to farmers, ensuring rapid increases of access to safe drinking water to the most vulnerable, and deploying seasonal forecasts to better anticipate drought could reduce the risks of future droughts, but long-term investments to address inequality are of equal importance.

Data availability
Almost all data will be available via the Climate Explorer.

References

All references are given as hyperlinks in the text.

Appendix

Table A1: USDM-based drought classifications and the corresponding thresholds from the different observed datasets used in the study.

US Drought Monitor-based classification	spi_th	cpc	chirps	mswep
D0 - abnormally dry	-0.4 to -0.8	3.06 - 3.33	2.83 - 3.09	2.82 - 3.08
D1 - moderate drought	-0.8 to -1.2	2.80 - 3.06	2.58 - 2.83	2.58 - 2.82
D2 - severe drought	-1.2 to -1.6	2.5 - 2.80	2.35 - 2.58	2.36 - 2.58
D3 - extreme drought	-1.6 to -2.0	2.34 - 2.56	2.14 - 2.35	2.1 - 2.36
D4 - exceptional drought	< -2.0	< 2.34	< 2.14	< 2.15